Internal tides off the Amazon shelf Part I: importance for the structuring of ocean temperature during two contrasted seasons

Fernand Assene [1], Ariane Koch-Larrouy [2], Isabelle Dadou [3], Michel Tchilibou [4], Guillaume Morvan [5], Jérôme Chanut [6], Alex Costa da Silva [7], Vincent Vantrepotte [8], Damien Allain [9], Trung-Kien Tran [10]

[1, 2, 3, 5, 9] Université de Toulouse, LEGOS (CNRS/IRD/UPS/CNES), Toulouse, France
[1, 6] Mercator Ocean International, 31400, Toulouse, France
[4] Collecte Localisation Satellites (CLS), 31500, Ramonville Saint-Agne, France
[7] Departamento de Oceanografia da Universidade Federal de Pernambuco, DOCEAN/UFPE, Recife, Brazil
[8, 10] Laboratoire d'Océanologie et de Géosciences (LOG), 62930, Wimereux, France

Correspondence to: Fernand Assene *fassene@mercator-ocean.fr*

Abstract

The impact of the tides (internal and barotropic) on the vertical and horizontal structure of temperature off the Amazon River is investigated over two highly contrasting seasons. Twinned regional simulations with and without tides are used to highlight the general effect of tides. The tides tend to cool down the ocean from the surface (~0.3 °C) to above the thermocline (~1.2 °C), and to thaw it below the thermocline (~1.2 °C). The heat budget analysis leads to the conclusion that vertical mixing could represent the dominant process that drives these temperature variations within the mixed layer, while it is associated with both horizontal and vertical advection below to explain temperature variations. The intensified mixing in the simulation including tides is attributed to the breaking of internal tides (ITs), on their generation sites over the shelf break and offshore along their propagation pathways. When over the shelf the mixing is attributed to the dissipation of the barotropic tides. Both horizontal and vertical advections exist in simulations without the tides but are strengthened when including it. Furthermore, vertical heat budget equation terms show a typical mode-1 horizontal propagation wavelength of ITs.

In addition, we found the tides can also have an impact on interactions between the upper ocean interface and the underlying atmosphere. They account for a significant proportion of the net heat flux between the atmosphere and the ocean, with a marked seasonal variation of 33.2% to 7.4% between the first and second seasons. Tidal dynamics could be therefore critical

to understand the regional climate. This study highlights the key role of tides, particularly, how ITs-related vertical mixing helps to shape ocean temperature off the Amazon.

Keywords: Amazon shelf break, internal tides, mixing, temperature, heat flux, modeling, satellite data.

I. Introduction

Temperature and its spatial structure carry out a crucial role in ocean dynamics, including water mass formation (Swift and Aagaard, 1981; Lascaratos, 1993; Speer et al., 1995), transport and mixing of other tracers in the ocean and exchanges with other biosphere compartments (Archer et al., 2004, Rosenthal et al., 1997), and most importantly on surface heat exchange at the interface with the atmosphere (Clayson and Bogdanoff, 2013; Mei et al., 2015) and can thus significantly influence the climate (Li et al., 2006; Collins et al., 2010). This oceanic thermal structure can be modified at various spatial and temporal scales. Through different processes external to the ocean like solar radiation, heat exchanges with the atmosphere, winds, precipitation, and freshwater inputs from rivers. And by its internal processes such as mass transport by currents and eddies (e.g., Aguedjou et al., 2021), mixing by turbulent diffusion (Kunze et al., 2012), internal waves and their dissipation (Barton et al., 2001; Smith et al., 2016; Salamena et al., 2021). Finally, bottom friction of the barotropic tidal currents may also produce intensified mixing especially for shallow water condition (e.g., over a shelf, see Lambeck and Runcorn, 1977; Le Provost and Lyard, 1997) and significantly modify ocean temperature in surface layers (Li et al., 2020).

The key source for internal waves generation is the barotropic or external tides. The external tides when interacting with sharp topography (e.g., ridge, sea mounts, shelf break) in a stratified ocean generate internal tides also called internal tidal/gravity waves, that may propagate and dissipate in the ocean interior causing diapycnal mixing (Baines, 1982; Munk and Wunsch, 1998; Egbert and Ray, 2000). The precise location of this dissipation is a big unknown. But evidence of dissipation at the generation sites, at the reflection to the bottom or close to the surface when the energy rays interact with the thermocline and pycnocline, have been measured and modelled (among others: Laurent and Garrett, 2002; Sharples et al., 2007, 2009; Koch-Larrouy et al., 2015; Nugroho et al., 2018; Xu et al., 2020 and Whalen et al., 2020). ITs may also dissipate or lose energy when they encounter others or when they interact with mesoscale or fine-scale structures (Vlasenko and Stashchuk, 2006; Dunphy and Lamb, 2014). Moreover, the surface interactions allow nonlinear internal solitary waves (ISW) to develop and

to propagate usually with phase-locked to the ITs troughs (New and Pingree, 1990, 2000; Azevedo et al., 2006; da Silva et al., 2011). Finally, ISW can dissipate and induce mixing (Sandstrom and Oakey, 1995; Feng et al., 2021; Purwandana et al., 2022). Moreover, ITs can vertically advect the water masses following their propagation. The effect is the vertical shifts in isopycnic levels of few meters to tens of meters, which can be observed in the thermocline (Wallace et al., 2008; Xu et al., 2020). But over a tidal cycle, the mean effect on temperature is null except some tidal residual circulation exists (Bessières, 2007).

Our study focuses on the oceanic region of northern Brazil off the Amazon River. This region exhibits a variation in the wind position and hence the position of the Intertropical Convergence Zone (ITCZ) during the year. This directly influences the discharge of the Amazon River, oceanic circulation, eddy kinetic energy (EKE) and the stratification (Muller-Karger et al., 1988; Johns et al., 1998; Xie and Carton, 2004). Hence, two very contrasting seasons form, April-May-June (AMJ) and August-September-October (ASO). AMJ (vs. ASO) season is characterized by an increasing (vs. decreasing) river discharge, stronger (vs. smaller) and shallower (vs. deeper) pycnocline. The North Brazilian Current (NBC) and eddy kinetic energy (EKE) are weaker (vs. stronger) (Aguedjou et al., 2019, Tchilibou et al., 2022). For the ASO season, the stronger NBC develops a retroflection (NBCR) between 5°–8° N that feeds the North Equatorial Counter-Current (NECC) transporting the water masses towards the east of the tropical Atlantic. The retroflexion also generates very large anticyclonic eddies (NBC Rings) exceeding 450 km in diameter (Didden and Schott, 1993; Richardson et al., 1994; Garzoli et al., 2004), which in turn transport water masses towards the Northern Hemisphere (Bourles et al., 1999a; Johns et al., 1998; Schott et al., 2003).

Internal tides are generated on the sharp shelf break which possesses a depth decreasing of 200-2000 m over some tens of kilometers (Fig.1). Six main sites (A to F) have been identified, with the most intense, A and B, located in the southern part of the region (Fig.1; Magalhaes et al., 2016, Tchilibou et al., 2022). Previous studies have shown that in this region ITs propagation is modulated by the seasonal variation of the currents (Magalhaes et al., 2016; Lentini et al., 2016; Tchilibou et al., 2022; de Macedo et al., 2023). In addition, seasonal variations in stratification induce changes in the internal tide's activity. With in AMJ (vs. ASO) a stronger (vs. smaller) energy conversion and a stronger (vs. smaller) local dissipation of ITs energy (Barbot et al., 2021, Tchilibou et al., 2022). Moreover, the interaction between the weaker (vs. stronger) background circulation and ITs can lead to less (vs. more) incoherent or non-stationary internal tides (Tchilibou et al., 2022). Incoherent ITs can account for about half

of the total internal tides in the global ocean and much more when looking at some regional ocean system. For example over 80% in equatorial Pacific (Zaron, 2017) and over 40% off the Amazon (see Fig.11e-f in Tchilibou et al., 2022). But quantifying the associated energy is difficult to determine and is still unknown in our region but is part of the scope of upcoming studies.

The role of ITs on the thermal structure of the ocean is of increasing interest with many studies in recent years. In the Hawaii shallow shelf surface waters, Smith et al. (2016) report that ITs can induce surface cooling from 1 °C to 5 °C. For the Indonesian region, ITs induce an annual mean surface cooling of 0.5 °C (Koch-Larrouy et al., 2007, 2008; Nagai and Hibiya, 2015 and Nugroho et al., 2018), that decreases local atmospheric convection, which in turn reduces precipitation by 20%. They can therefore fulfils a relevant role on regional climate (Koch-Larrouy et al., 2010, Sprintall et al., 2014, 2019). Furthermore, in the Andaman Sea, Jithin and Francis (2020) showed that ITs can affect the temperature in deep waters (> 1600 m), leading to a warming of about 1–2 °C. But off the Amazon plateau, the impact of ITs on the thermal structure of the ocean is still poorly understood.

During the ASO season, cold water (< 27.6 °C) associated with the western extension of the Atlantic Cold-water Tongue (ACT) enter the region from the south and run along the edge of the continental shelf to about 3°N, establishing a cold cell often referred to as seasonal upwelling (Lentz and Limeburner, 1995; Neto and da Silva, 2014). Modelling studies, with and without tides, have shown that this upwelling is affected by the tides. Cooling is more realistic when tides are included (Ruault et al., 2020). However, these analyses cannot determine what processes are at work. For example, it is not yet explicit whether the tidal-induced cooling is due to mixing on the shelf produced by barotropic tides, or to the mixing produced by baroclinic tides at their generation sites and propagation pathways. Neto and da Silva (2014), based on *in situ* observations, suggest instead that it is the vertical advection triggered by the NBC that can explain the cooling observed at the surface. Following on from the latter, we can also examine the role of horizontal advection and its contribution relative to vertical advection.

To answer the previous questions, we used a high-resolution model (1/36°) with and without explicit tidal forcing and a satellite SST product, with the aim of highlighting the impact of tides on the temperature structure and quantify the associated processes. We distinguish the analysis for the two contrasted seasons (AMJ and ASO) described above. The SST product, our model, and the methods used are described in section II. The validation of certain characteristics of the barotropic and baroclinic tides and of the temperature is presented in section III. The

impacts of ITs on the temperature structure, the influence on heat exchange at the atmosphere-ocean interface, and the processes involved, are analyzed in section IV. The discussion and the summary of the obtained results are presented in section V and VI respectively.

II. Data and Methods

II.1. Satellite Data used: TMI SST

This dataset derived from Tropical Rainfall Measurement Mission (TRMM), which performs measurements using onboard TRMM Microwave Imager (TMI). The microwaves can penetrate clouds and are therefore crucially important for data acquisition in low latitude regions, cloudy covered during long periods of raining seasons. We use Remote Sensing Systems (RSS) TMI data products v7.1, which represents the most recent version of TMI SST. It contains a daily mean of SST with a 0.25°×0.25° grid resolution (~25 km). This SST is obtained by inter-calibration of TMI data with other microwave radiometers. The TMI SST full description and inter-calibration algorithm are detailed in Wentz et al., (2015).

II.2. The NEMO Model: *AMAZON36* configuration

The numerical model used in this study is the Nucleus for European Modelling of the Ocean (NEMOv4.0.2, Madec et al., 2019). The configuration designed for our purpose is called *AMAZON36* and covers the western tropical Atlantic region from the Amazon River mouth to the open ocean. Other configurations exist in this region, but either they have a coarse grid (¼° , Hernandez et al., 2016), or when the grid is fine (1/36°) they do not extend very far eastwards and therefore exclude most of the site B (Ruault et al., 2020). The current configuration avoids these two limitations. The grid resolution is fine (1/36°) and the domain lies between 54.7°W–35.3°W and 5.5°S–10°N (Fig.1). In this way, we can capture the internal tides radiating from all the generating sites on the Brazilian shelf break. Unlike previous configurations, we do not use multiple nested grids, but a single fine grid. The vertical grid comprises 75 vertically fixed z-coordinates levels, with a narrower grid refinement near the surface with 23 levels in the first 100 m. Cell thickness reaches 160 m when approaching the bottom. The horizontal and vertical resolutions of the grid are therefore fine enough to resolve low-mode internal tides. This grid resolution has already been used for this purpose in this region (e.g., Tchilibou et al., 2022).

A third order upstream biased scheme (UP3) with built-in diffusion is used for momentum advection, while tracer advection relies on a 2nd order Flux Corrected Transport (FCT) scheme (Zalesak, 1979). A Laplacian isopycnal diffusion with a constant coefficient of 20 $m^2.s^{-1}$ is used for tracers. The temporal integration is achieved thanks to a leapfrog scheme

combined with an Asselin filter to damp numerical modes, with a baroclinic time step of 150 s. The $k-\varepsilon$ turbulent closure scheme is used for the vertical diffusion coefficients. Bottom friction is quadratic with a bottom drag coefficient of 2.5×10^{-3}, while lateral wall free-slip boundary conditions are prescribed. A time splitting technique is used to resolve the free surface, with the barotropic part of the dynamical equations integrated explicitly.

We use the 2020's release of the General Bathymetric Chart of the Oceans (GEBCO 2020, see details in https://www.gebco.net/data_and_products/gridded_bathymetry_data/gebco_2020/) interpolated onto the model horizontal grid, with the minimal depth set to 12.8 m. The model is forced at the surface by the ERA-5 atmospheric reanalysis (Hersbach et al., 2020). The river discharges are based on monthly means from hydrology simulation of the Interaction Sol-Biosphère-Atmosphère model (ISBA, see description in https://www.umr-cnrm.fr/spip.php?article146&lang=en) and are prescribed as surface mass sources with null salinity, and we use a multiplicative factor of 90% based on a comparison with the HYBAM interannual timeseries (HYBAM, 2018). The model is forced at its open boundaries by (i) the fifteen major tidal constituents (M2, S2, N2, K2, 2N2, MU2, NU2, L2, T2, K1, O1, Q1, P1, S1, and M4) and (ii) barotropic currents, both derived from FES2014 atlas (Lyard et al., 2021). In addition to the open boundaries, we prescribe the recent MERCATOR-GLORYS12 v1 assimilation data (Lellouche et al., 2018) for temperature, salinity, sea level, current velocity and derived baroclinic velocity.

The simulation was initialized on the 1st of January 2005, and ran for 11 years until December 2015. In this study, we use 3-years model outputs from January 2013 to December 2015. Indeed, the model has reached an equilibrium in terms of seasonal cycle after 2 years of run. A twin model configuration without the tides is used to highlight the influence of tides on the temperature structure. To assess the realism of the model, we perform validation of various state variables used in this study such as the current's circulation, temperature, salinity, stratification as well as the barotropic and baroclinic tides properties.

II.3. Methods

II.3.1. Barotropic/baroclinic tide separation and tide energy budget

We follow Kelly et al. (2010) to separate barotropic and baroclinic tide constituents: pressure, currents and energy flux. There is no separation following vertical propagation modes. Then we analyze the total energy for all the resolved propagation modes for a given harmonic.

Note that the barotropic/baroclinic tide separation is performed directly by the model for better accuracy. Even though, it has the disadvantage of being very costly in terms of computing time. We have therefore only analyzed the M2 harmonic for the single year 2015. Note that M2 is the major tidal constituent in this region (Prestes et al., 2018; Fassoni-Andrade et al., 2023). It represents ~70% of the tidal energy (Beardsley et al., 1995; Gabioux et al., 2005).

The barotropic and baroclinic tide energy budget equations are obtained by ignoring as a first-order approximation, the energy tendency, the nonlinear advection and the forcing terms (Wang et al., 2016). Then, the remaining equations are reduced to the balance between the energy dissipation, the divergence of the energy flux, and the energy conversion from barotropic to baroclinic (e.g., Buijsman et al., 2017; Tchilibou et al., 2018, 2020; Jithin and Francis 2020; Peng et al., 2021) :

$$D_{bt} + \nabla_h \cdot F_{bt} + C \approx 0 \quad (1)$$

$$D_{bc} + \nabla_h \cdot F_{bc} - C \approx 0 \quad (2)$$

bt and bc indicate the barotropic and baroclinic terms, D is the depth-integrated energy dissipation, which can be understood as a proxy of the real dissipation since D may encompass the energy loss of other tidal harmonics, non-linear terms and/or numerical dissipation (see Nugroho et al., 2018), $\nabla_h \cdot F$ represents the divergence of the depth-integrated energy flux, whilst C is the depth-integrated barotropic-to-baroclinic energy conversion, i.e., the amount of incoming barotropic energy converted into internal tides energy over the steep topography, with:

$$C = \langle \nabla H \cdot U_{bt}^* P_{bc}^* \rangle \quad (3)$$

$$F_{bt} = \langle U_{bt}^* P_{bt} \rangle \quad (4)$$

$$F_{bc} = \int_H^{\eta} \langle U_{bc}^* P_{bc} \rangle \, d_z \quad (5)$$

where the angle bracket $\langle \cdot \rangle$ denotes the average over a tidal period, ∇H is the slope of the bathymetry, U^* is the current velocity (u, v) respectively in (x, y) directions, P_{bc}^* is the baroclinic pressure perturbation at the bottom, H is the bottom depth, η the surface elevation, P is the pressure, then F is the energy flux and emphasizes the pathway of the respective tides (external or internal).

II.3.2. 3-D heat budget equation for temperature

The three-dimensional temperature budget was computed online and further analyzed. It is the balance between the total temperature trend and the sum of the temperature advection, diffusion and solar radiative and non-solar radiative fluxes (e.g., Jouanno et al., 2011; Hernandez et al., 2017):

$$\partial_t T = \underbrace{-u\partial_x T - v\partial_y T - w\partial_z T}_{ADV*} \underbrace{- \partial_z(K_z \partial_z T)}_{ZDF} + LDF_T + FOR_Z + Numdiff \quad (6)$$

Here T is the model potential temperature, *(u, v, w)* are the velocities component in the (x, y, z) [respectively eastward, northward and upward] directions, $ADV*$ *is* the 3-D tendency term from the advection routine of the NEMO code (from the left to right: zonal, meridional and vertical terms). Note that this term hides secondary terms that are important to define here. Hence, the total advection tendency of temperature (ADV) is expressed as follows:

$$ADV = \underbrace{\langle U \cdot \nabla T \rangle}_{ADV*} + \underbrace{\langle U' \cdot \nabla T \rangle + \langle U \cdot \nabla T' \rangle + \langle U' \cdot \nabla T' \rangle}_{Non-Linear\ terms} + Numdiff_{ADV} \quad (7)$$

where U' is the tidal current, and T' represents the anomaly of temperature that is produced by the tides apart the advection. When comparing the tidal and non-tidal simulation, the residual term could come from at least three possible tidal impacts :

1) The result of the advection is null over a tidal cycle except in some tidal residual circulation. In our region the residual tidal circulation is limited but might be slightly more important on the shelf (Bessières et al., 2008).

2) In the nonlinear terms of the previous equation (7), temperature could be modified by other processes than advection, which will count in the total tendency and mark the signature of the impact of the tides.

3) Finally, and it might represent the key point, in the model, the advection term leads to some diffusivity of the temperature due to numerical dissipation of the advection scheme ($Numdiff_{ADV}$), in contrast to some non-diffusive advection scheme like in Leclair and Madec (2009). In our case, we are using the FCT advection scheme that includes a diffusive part (Zalesak, 1979). In previous study, this mixing has been quantified to be responsible for 30% of the dissipation (in lower resolution 1/4° resolution, Koch-Larrouy et al., 2008), as part of the

high-frequency work of the advection diffusion. We except here at 1/36° that this effect will be smaller but still non negligible. Explicit separation of these 3 impacts is beyond the scope of our study but will be discussed in the last section.

Furthermore, ZDF represents the vertical diffusion, LDF_T is the lateral diffusion, FOR_z is the tendency of temperature due to penetrative solar radiation and includes a vertical decaying structure. At the air-sea interface, the temperature flux is equal to the non-solar heat flux (sum of the latent, sensible, and net infrared fluxes). FOR_z can modify temperature in the thin surface layer but will be unshown in the following. $Numdiff$ corresponds to the numerical diffusion for the temperature.

III. Model validation

In this subsection, we assess the quality of our model's simulations by verifying whether they are in good agreement with the observations and other reference data. Firstly, for the barotropic and baroclinic characteristics of the M2 tides for the year 2015, and finally for the temperature for the period from 2013 to 2015.

III.1. M2 Tides in the model

We initially examined at the barotropic SSH and there is a good agreement in both amplitude and phase between FES2014 and the model, Fig2a and Fig.2b respectively. Nevertheless, near the coast, some differences are observed in amplitude. The SSH amplitude of the model is lower (~ +50 cm) north of the mouth of the Amazon. However, shorewards and on the southern part of the mouth, the model overestimates the amplitude by ~ +20 cm and ~ +40 cm respectively. These biases are of the same order of magnitude as Ruault et al. (2020). The flux of the barotropic tidal energy flowing inshore is represented by the black arrows in Fig.2c and Fig.2d for FES2014 and the model respectively. A fraction of this energy is converted into baroclinic tidal energy over the steep slope of the bathymetry. We compared the depth-integrated barotropic-to-baroclinic energy conversion rate (C) between FES2014 and the model, color shading in Fig.2c and Fig.2d respectively. The model does reproduce the same conversion patterns of FES2014 over the slope, but hardly offshore over the Mid-Atlantic Ridge between 42°W–35°W and 7°N–10°N. This leads to an overall underestimate of about 30%. It is worth noting that C increases with bathymetry resolution. The latter therefore plays a critical role in converting barotropic tidal energy into internal tides (see Niwa and Hibiya, 2011). Compared with FES2014 (~1.5 km), the horizontal grid of our model is coarser (~3 km).

Meaning that the difference in bathymetry resolution could explains the difference in energy conversion with FES2014. Later, another part of the barotropic energy is dissipated on the shelf by bottom friction and induces mixing from the bottom (Beardsley et al., 1995; Gabioux et al., 2005; Bessières, 2007; Fontes et al., 2008). Most of the dissipation of barotropic energy (D_{bt}) occurs in the middle and inner shelf between 3°S–4°N (Fig.2e) in good agreement with Beardsley et al. (1995) and Bessières (2007). The remaining barotropic energy flows over hundreds of kilometers into the estuarine systems of this region (Kosuth et al., 2009; Fassoni-Andrade et al., 2023).

For the baroclinic tides, the critical parameter, $\gamma = s/\alpha$, is defined as the ratio between the slope of the bathymetry, $s = \nabla H$ (see Fig.1), and the slope of the radiated internal wave, $\alpha = \sqrt{(\omega^2 - f^2)/(N^2 - \omega^2)}$, with ω the tidal frequency for a given wave, f is the Coriolis frequency and N^2 represents the squared Brünt-Väisälä frequency near the bottom (e.g., Nash et al., 2007; Vic et al., 2019). On the slope where ITs are generated, $\gamma > 1$, meaning that the topography is supercritical. Consequently, the baroclinic tides, once generated, will propagate in the opposite direction to the barotropic tides, i.e., from the slope towards the open ocean, as shown by the model's baroclinic energy flux (F_{bc}), black arrows in Fig.2f. F_{bc} highlights the existence of six main sites of ITs generation on the slope. Two of these are more important (A and B) regarding their higher and far extended energy flux, in good agreement with Magalhaes et al. (2016), Barbot et al. (2021) and Tchilibou et al. (2022). From these two main sites, ITs propagate for the nearly 1000 km. Along the propagation pathways, they can dissipate their energy. Color shading in the Figure-2f shows the model's depth-integrated internal tides energy dissipation (D_{bc}). We first look at the local dissipation of this energy defined as $q = D_{bc}/C$ (see Laurent and Garrett, 2002). q is integrated over the slope in the same boxes as defined in Table A1 in Tchilibou et al. (2022). This reveals that a significant part of the energy, about 30%, is dissipated locally in the different boxes in good agreement with the latter study. The remaining part of the energy is exported offshore, and it is dissipated along the propagation path. This offshore dissipation is more extensive along path A, ~300 km from the slope, with two patterns spaced approximately by an average wavelength of 120–150 km corresponding to mode-1 propagation. The offshore dissipation is less extensive along path B, occurring around 100–200 km from the slope (Fig.2f).

Another critical characteristic of internal tidal waves is their SSH imprints along the propagation pathway. We compared an estimate of this signature deduced from the altimeter

tracks (Fig.2g) produced by Zaron (2019) with our model (Fig.2h). The model is in good agreement with this product, with an overestimation of the order of ~ +1.5 cm on the SSH maxima. It is relevant to note the baroclinic SSH of the model is an average over the year 2015, whilst the estimate is an average over about 20 years. This more extended period may lower the amplitude of the signal obtained from the altimetry observations. Furthermore, the variability within the two datasets is not the same. This may explain some differences in the positioning and amplitude of the maxima.

Only the energy dissipation of the M2 tides is presented above. Elsewhere, the harmonic analysis does not consider the incoherent (non-stationary) part of the tidal energy, which has been found to be non-neglectable (Tchilibou et al., 2022). And can therefore influences the structure of the temperature. Further on, the analysis are carried out on a seasonal scale, which means that the mean temperature field obtained could result from the cumulative effect of all coherent and incoherent tidal harmonics.

III.2. Temperature validation

For the following, it should be noted we obtained the bias between TMI SST and the two model simulations after linear interpolation of the model data into the observation grid.

Figure 3 shows the mean SST over the entire period 2013–2015 from TMI SST (Fig.3a), the tidal simulation (Fig.3b) and the non-tidal simulation (Fig.3c). The simulation with tides accurately reproduces the spatial distribution of the observations both for cooling on the shelf around 47.5°W and to the southeast between 40°W –35°W and 2°S–2°N, as shown by the weak bias, < ±0.1°C, with TMI (Fig.3d). This cooling is inaccurately reproduced by the non-tidal simulation which exhibits a warm bias of about 0.3 °C (Fig.3.e). To the northeast, between 50°W–54°W and 3°N–8°N in the Amazon plume, the SST of the non-tidal simulation is in better agreement with the observations, while the SST of the tidal simulation is about > 0.6 °C cooler than TIM SST (Fig.3d). Such a difference fits to what is obtained by other models in the same region (e.g., Hernandez et al., 2016, 2017; Gévaudan et al., 2022). Far offshore, between 50°W–40°W and 6°N–10°N, both simulations reveal a negative bias of about 0.2–0.3 °C (Fig.3d-e). We averaged the observations and the interpolated model data in the corresponding dashed line box in the upper panels, with depth < 200 m masked. This location is around the ITs generation sites and on part of their pathways. Then, we compute the seasonal cycle of the three products (Fig.3f). The tidal and non-tidal simulations of the model reproduce accurately both the seasonal cycle and the standard deviation of the observations, with a low RMSE of ~10^{-2} °C between each simulation and TMI SST (Fig.3f). This indicates the robustness of our

model simulations. Nevertheless, over the seasonal cycle, it appears that between January-April and July-December, the tidal simulation is closer to the observations, while the non-tidal simulation seems moderately warmer than the observations. In May-June, both simulations are colder than TMI SST (Fig.3f).

To gain an insight into our model along the depth, we used the mean model water properties (salinity and temperature) for the three years 2013-2015 in the same region as in Fig.3f. We compared them with the WOA2018 climatological (2005–2017) data (https://www.ncei.noaa.gov/access/world-ocean-atlas-2018/). We used hereabove and elsewhere $\sigma_\theta[\rho - 1000]$ to represent the density, with ρ the water density. Figure 3g shows the Temperature-Salinity (T-S) diagram, with equal density (σ_θ) contours, for WOA2018 (black line), tidal simulation (blue line) and non-tidal simulation (red line). Both simulations exhibit similar pattern with WOA2018 for deeper waters, i.e., T < 17 °C and σ_θ > 25.6 kg.m^{-3}. However, there exist minor discrepancies for the surface layer waters, i.e., T > 17 °C and 22.4 > σ_θ < 25.6 kg.m^{-3}. At that level, the tidal simulation better reproduces the T-S profiles. The water is slightly more eroded in the non-tidal simulation. These petty differences between WOA2018 observations and the model, even more with the tidal simulation, further demonstrate the ability of our model to reproduce the observed water mass properties.

IV. Results

In this section, we present the influence of tides on the temperature, the associated processes, and the impact on the atmosphere-ocean net heat. The analyses were performed on a seasonal scale between April-May-June (AMJ) and August-September-October (ASO) for the three years 2013-2015.

IV.1. Tide-enhanced surface cooling

During the first season, warm waters, > 27.6°C, dominate near the coast, especially in the middle shelf and in the south-east. While cold waters are present offshore north of 6°N (Fig.4a-c). Off the mouth of the Amazon River, water colder than 28.2 °C spread between 43°W–51°W for TMI SST (Fig.4a) and the tidal simulation (Fig.4b), whilst warmer waters are present in the same area for the simulation without the tides (Fig.4c). Figures 4d-f show the SST, averaged over the ASO season. The TMI SST observations (Fig.4d) shows an upwelling cell represented by the extension of the 27.2 °C isotherm (white dashed contour) along the slope to about 49°W–3°N towards the north-east of the region, which forms the extension of the ACT. This extension also exists in the tidal simulation (Fig.4e), whereas ≤ 27.2 °C waters are not

crossing 45.5°W and remain in the southern hemisphere in the simulation without the tides (Fig.4f). Which means that a lesser upwelling cell may exist without the tides, and it is enhanced by -0.3°C in average due to tidal effect. The tides allow waters colder than 27.2°C to form further north-east. Finally, we can note that the mean SST shows a very contrasting distribution between the two seasons. There are warm waters along the shelf and cold waters offshore during the AMJ season (Fig.4a-c). This is followed by warming along the Amazon plume and offshore, and a upwelling cells in the south-east (Fig.4d-f).

The general impact of the tides, illustrated by the SST anomaly between the tidal and the non-tidal simulation, is a cooling over a large part of the study area with maxima up to 0.3 °C (Fig.5a-b). For ASO, tides induce a warming (> 0.3 °C) on the shelf at the mouth of the Amazon River (Fig.5b), while for AMJ it is a cooling of the same intensity (Fig.5a). That difference will be further discussed. Out of the shelf, the temperature anomaly for each season has different spatial structures. This is probably due to a different mesoscale variability between the two seasons.

IV.2. Impact of the tides in the atmosphere-to-ocean net heat flux

The atmosphere–ocean net heat flux (Qt) reflects the balance of incoming and outgoing heat fluxes across the atmosphere-ocean interface (see details on Moisan and Niiler, 1998; Jayakrishnan and Babu, 2013). During AMJ, the tides mainly induce positive Qt anomalies over the whole domain. The average values are around 25 $W.m^{-2}$ in the plume and the Amazon retroflection to the northeast and along A and B (Fig.5c). Negative SST anomalies (~0.3°C) occur throughout the domain in the same location. During the ASO season, at the mouth of the Amazon, there are negative Qt anomalies but of same magnitude as during the previous season (Fig.5d). At this location, positive temperature anomalies (~0.3°C) are observed (Fig.5b). Elsewhere, there are positive Qt anomalies and negative SST anomalies. It therefore appears that negative SST anomalies induce positive Qt anomalies and vice versa. Hence, the spatial structures of Qt anomalies and SST anomalies fit almost perfectly together for the respective season. As it is shown by the correlation among them. There is a strong negative correlation of 0.97 with a significance of $R^2 = 0.95$ for the AMJ season. And roughly the same intensity and sign for the ASO season with 0.98 and 0.96, respectively for the correlation and its significance (Fig.5e). This is consistent with the fact that the atmosphere and the underlying ocean are balanced. Then, the SST cooling induced by upwelled cold water will try upset this balance. As a result of this, an equivalent variation in the net heat flux from the atmosphere to the ocean will attempt to restore it.

The integral over the entire domain of the net heat flux for each season and for each simulation is shown in Figure 5f. During the AMJ season, Qt increases from 23.85 TW (1 TW = 10^{12} W) for the non-tidal simulation to 35.7 TW for the tidal simulation, i.e., an increase of 33.2 %. The tides are behind a third of Qt variation. This is very large compared to what is observed elsewhere in other ITs hotspots (e.g., 15% in Solomon Sea, Tchilibou et al., 2020). During the second season, there is a smaller increase in Qt of about 7.4% between the two simulations, i.e., from 73.03 TW to78.83 TW for the non-tidal and tidal simulations respectively (Fig.5f).

Moreover, it is also worth noting the significant difference in integrated Qt between the two seasons. The values are less than 36 TW during the AMJ season, whereas they are around twice as high, > 73 TW, during the ASO season. Given that colder SST induce a stronger Qt, these higher values are likely related to the arrival of water from ACT, which forms upwelling cells (Fig.4d-f) with a secondary tidal effect.

IV.3. Vertical structure of Temperature along internal tides pathway

To further analyze the temperature changes between both simulations, we made vertical sections following the path of ITs emanating from sites A and B (respectively black and red line in Fig.2e). Hereunder, (i) only the transects following the pathway A will be shown, since the vertical structure is similar following pathway B especially for AMJ season, or because some processes tend to be null along pathway B during the ASO season. (ii) The mixed layer refers to a quasi-homogenous surface layer of temperature-dependent density that interacts with the atmosphere (Kara et al., 2003). Its maximum depth also known as mixed-layer depth (MLD) is defined as the depth where the density increases from the surface value, due to temperature change of $|\Delta T| = 0.2\ ^{\circ}C$ with constant salinity (e.g., Dong et al., 2008; Varona et al., 2019).

Figure 6 shows the vertical sections of temperature for the two seasons following A. For the AMJ season, over the slope and near the coast, cold waters (< 27.6 °C) remain below the surface at ~20 m for the tidal simulation (Fig.6a) and deeper at ~60 m for the non-tidal simulation (not shown). Then, cold waters rise to the surface more than 400 km offshore for both simulations. Although at the surface the SST anomaly is relatively small (~ -0.3 °C, Fig.5a), because the SST is likely damped by the heat fluxes, further down the water column, this anomaly becomes much larger (Fig.6b). Note that cyan and yellow dashed lines in Fig.6b and Fig.7b refer to thermocline for tidal and non-tidal simulations respectively. Above that thermocline (< 120 m), the simulation with the tides is colder by 1.2 °C from the slope where the ITs are generated to the open ocean following their propagation path. Conversely, below

the thermocline, the tidal simulation is warmer by approximately the same intensity (1.2 °C) up to ~300 m depth and along the propagation path (Fig.6b). During this AMJ season, the thermocline is ~100 m ± 15 m deep and the MLD is ~40 m ± 20 m deep (dashed white line, Fig.6a). They both have a very weak slope between the coast and the open ocean. Over the whole domain, the thermocline is deeper by about 15 m on average in the non-tidal simulation, following the propagation paths of the ITs, on the Amazon shelf and plume (Fig.6c). Whilst MLD in the non-tidal simulation is deeper by an average of 10 m over the shelf, 4 m on average along the ITs propagation paths and close to zero in the Amazon plume (Fig.6d).

During the ASO season, cold waters previously confined below the surface during the previous season (AMJ) rise to the surface. These cold waters extend over the slope and up to about 150 km offshore in the non-tidal simulation (not shown) and up to 250 km offshore in the tidal simulation (Fig.7a). The 27.2 °C isotherm only reaches the surface above the slope in the tidal simulation and remains below the surface (~30 m) in the non-tidal simulation. This aligns with the missing of that isotherm at this location in the corresponding SST map (Fig.4e). For the tidal simulation, at the surface, the temperature is therefore colder than in previous season. The temperature anomaly in the ASO season is smaller (< 0.4 °C, Fig.7b) in the surface layers (< 40 m) near the coast compared to the AMJ season (Fig.6b). In contrast, during the ASO season, this cooling can reach the surface and results in a colder SST along A (-0.3 °C, Fig.5a) . The strongest cooling of ~ -1.2 °C is deeper between 60 and 140 m depth. Below the thermocline, a warming of about 1.2 °C is also present but extends less offshore to about 650 km, Fig.7b (vs. ~1000 km, Fig.6b). During this ASO season, the coastward slope of the thermocline and MLD becomes somewhat steeper compared to the other season. In both simulations, there is a dip of ~80 m, i.e., ~60 m offshore and ~140 m inshore, for the thermocline (dashed black line, Fig.7a). And a dip of ~40 m, i.e., ~30 m offshore and ~70 m inshore, for MLD (dashed white line, Fig.7a). Over the entire domain, the tides shallow the thermocline depth by ~6 m on the shelf and ~12 m at the plume and far offshore along the propagation path of A (Fig.7c). They shallow MLD in the tidal run by about 10 m along the shelf and ~4 m along the propagation path of A (Fig.7d).

Between the two seasons, there is also a change in the vertical density gradient (Stratification) between the coast and the open sea. In the tidal simulation, during the AMJ season, the isodensities are tight near the coast and thicken towards the open sea (Fig.6a). This means that a strong stratification is present near the coast and decreases towards the open sea. In contrast, during the second ASO season, the isodensities are thicker near the coast and tight

offshore (Fig.7a). As the result of this, the stratification is weaker inshore than offshore. This clearly highlights a seasonality in the vertical density gradient profile in agreement with Tchilibou et al. (2022). Note that, this behavior also appears in the simulation without the tides (not shown). The transects of the temperature anomaly, Fig.6b and 7b, show that ITs and likely the barotropic tides can influence the temperature in the ocean from the surface to the deep layers, with a greater effect on the first 300 meters. One question we address in this paper is to better understand what processes are at work that explain these temperature changes.

IV.4. What are the processes involved?

To explain the observed surface and water column temperature changes, we computed and analyzed the terms of the heat balance equation (see Section II.3.2, Equation 6) for both seasons (AMJ and ASO) averaged over the three years from 2013 to 2015.

IV.4.1. Vertical diffusion of Temperature

Figure 8 shows the vertical temperature diffusion tendency (ZDF). ZDF is averaged between 2–20 m, i.e., within the mixed-layer. For the AMJ season, ZDF in tidal simulation (Fig.8a) shows a negative trend (cooling) in the whole domain. The maximum values (> |0.4| °C.day^{-1}) are located along the slope where the ITs are generated and on their propagation path. There is a larger horizontal extent along A of ~700 km from the coasts compared to B, where it is ~300 km from the coasts. Elsewhere, it remains very low, > -0.1 °C.day^{-1}. For the non-tidal simulation (Fig.8b), the ZDF is very weak over the entire domain (>> -0.1 °C.day^{-1}). For the ASO season, the tidal simulation (Fig.8c) shows a decrease of the ZDF near the coast (< 100 km) and a strengthening offshore along A compared to the previous season, but with the same cooling trend (< -0.4 °C.day-^{1}). Along B, it tends to be null, both at the coast and offshore (Fig.8c). In addition, the mesoscale circulation and eddy activity intensify during this season. To the northeast, approximately between 4°N–8°N, and 47°W–53°W, there is a cooling on the shelf of ~0.3 °C.day^{-1} with eddy-like patterns in the tidal simulation (Fig.8c). The processes by which these features might arise will be examined in more detail in the section V. Unsurprisingly, ZDF is very weak elsewhere for the non-tidal simulation (Fig.8d). Whatever, the ITs could be the dominant driver of vertical diffusion of temperature along the shelf break and offshore, while the barotropic tides could prevail on the shelf to explain the weak ZDF values.

On the vertical following A, we have noted inverted ZDF values, with mean magnitude of ~ |0.4| °C.day^{-1}. These values are centered around the thermocline for the simulation with

tides in the two seasons AMJ and ASO (respectively Fig.8e and 8f). There is a cooling trend above the thermocline and a warming trend below. The average vertical extension is up to ~350 m depth for the maximum values but exceeds 500 m depth for the low values (< 0.1 °C.day^{-1}). As for the horizontal averages (Fig.8a and 8c), from one season to another there is a weakening of ZDF above the slope and a strengthening offshore, Fig.8e and 8f, for AMJ and ASO respectively. Furthermore, offshore ZDF maxima seem to be discontinuous and spaced of about 140–160 km during the AMJ season (Fig.8e) but are more continuous for the ASO season (Fig.8f). For the non-tidal simulation, the mean ZDF tends to be null in the ocean interior but remains quite large (> -0.2 °C.day^{-1}) in the thin surface layer during the two seasons (Fig.8g-h).

Furthermore, it is worth to note that along the ITs propagation's pathway, the maximum of the ZDF follows the maxima of the baroclinic tidal energy dissipation (color shading in Fig.2f). Thus, the dissipation of ITs causes vertical mixing that enhances the cooling observed at the surface. In addition, this temperature diffusion contributes to greater subsurface cooling, and warming in the deeper layers beneath the thermocline.

In section IV.3, the seasonality of the stratification was highlighted, which we recall is stronger at the coast relative to the open ocean during the AMJ season, and reverses during the ASO season to become stronger offshore relative to the coast. This could explain why the ZDF is stronger along the slope and the near-coastal pathway B during the AMJ season (Fig.8a and 8e). And why it is weaker along the slope, close to zero following B, and reinforce offshore of A during the ASO season (Fig.8c and 8f). Previous studies have shown that stratification influences the generation of ITs and controls their propagation modes. Here we show that stratification also plays a role on the fate of these ITs, in this case on their dissipation. The stratification could determine where ITs waves dissipate their energy in the water column, as mentioned by de Lavergne et al. (2020).

IV.4.2. Advection of temperature

The vertical (z–ADV) or horizontal (h–ADV) terms of the temperature advection tendency are also averaged between 2–20m, for each season over the three years. Remember that when comparing the tidal and non-tidal simulation, a residual term may arise (see equation 7 in the section II.3.2) and must be considered for the following terms, even if it is expected to be low.

IV.4.2.a Vertical advection of Temperature

z-ADV is almost null in these surface layers throughout the region (Fig.9a-d). For both seasons, some weak extreme values are in the northwest on the plateau between 54°W–50°W and 3°N–3°N and are for the same intensity between the two simulations with and without tides. This result suggests that, overall, the tides fail to generate vertical temperature advection within these ocean surface layers. At deeper depth, z–ADV tendency term is non negligible, and clearly higher in tidal simulation than in non-tidal one. Vertical sections (Fig.9a-h) show an intensification of z-ADV of about ±0.8°C.day^{-1} located below the MLD (magenta dashed line) and seems to be centered around the thermocline (black dashed line), with a vertical extension from 20–200 m depth. z-ADV is stronger in tidal simulation during the both seasons (Fig.9e-f) and mainly presents sparse extrema offshore (> 300 km) for the non-tidal simulation (Fig.9g-h). For the simulation with the tides, z-ADV appears to be rather dominated by a cooling trend, with a marked hotspot on the slope followed by other hotspots offshore. These extreme values are spaced about 120–150 km apart, i.e., the imprint of mode-1 propagation wavelength as for the baroclinic tidal energy dissipation (Fig.2f). For the both simulations (Fig.9e-h), the extreme values are located within the narrow density (σ_θ) contours [23.8–26.2 kg.m^{-3}], i.e., they follow the maximum of the stratification, namely, the pycnocline.

IV.4.2.b Horizontal advection of temperature

Horizontal advection of temperature (h–ADV) is defined as the sum of the zonal (x–ADV) and meridional (y–ADV) terms of temperature advection tendency. As for z–ADV, the mean of h–ADV tends to be null over the entire domain in the surface layers for both seasons in both simulations (Fig.10a-d). Nevertheless, some weak extreme values are in the northwest of the plateau between 54°W–50°W and 3°N–3°N. That intensify during the ASO season in both simulations, ~ ±0.2 °C.day^{-1}, Fig.10c and 10d for the tidal and non-tidal simulations respectively. During AMJ, h–ADV is slightly stronger, ~0.1 °C.day^{-1}, around sites A and B in the tidal simulation (Fig.10a) than in the non-tidal simulation (Fig.10b). This appears to be related to the ITs generated along the slope. On the other hand, the small difference between the two simulations in the surface layers shows that the tides hardly generate h–ADV. Then, h–ADV could not influence the cold-water tongue observed over the surface SST during the ASO season (Fig.4d-f). This result aligns with Bessières et al. (2008), which had previously shown that the tidal residual mean transport is null in the upwelling region in the south-east and low (< |0.1| Sverdrup) over the whole shelf.

Along the vertical following A, h-ADV maxima remain essentially confined below the mixed-layer depth, with much more intense values in the tidal simulation (Fig.10e-f) compared to the non-tidal simulation (Fig.10g-h). h–ADV contributes to both warming and cooling of the temperature of ~ ±0.4 °C.day^{-1} from the slope to more than 500 km offshore. During both seasons, the average vertical extension lies between the surface and 400 m depth for the tidal simulation and a little less extended between 20–300 m depth for the non-tidal simulation. As for z-ADV, h–ADV is also stronger within the pycnocline. For the tidal simulation, there is a warming above the slope (0.4 °C.day^{-1}) reaching the surface in both seasons. This vertical excursion is observed elsewhere for ZDF and z–ADV, and it is probably a marker of local dissipation of ITs at their generation site. The local dissipation of ITs clearly affects both advection and vertical diffusion of the temperature. But there are very low values along the slope when averaging h–ADV or z–ADV between 2–20 m and much more strong values for the ZDF. This means that the energy dissipated by ITs is mostly transferred to mixing.

Furthermore, unlike ZDF and z–ADV, the (horizontal) location of h-ADV maxima mismatch the dissipation hotspots. It is difficult to identify the wave-like characteristic of the propagation of ITs in h-ADV. This probably means that ITs hardly induce any horizontal motion of water mass. We can therefore deduce that the observed increase in h-ADV is mainly because of the barotropic tides.

V. Discussion

V.1. Vertical advection tendency term

Results showed that z-ADV is stronger in the deeper layer, below the MLD and within the pycnocline (Fig.9e-h). As mentioned above, this tendency term includes both nonlinear effect between the temperature and the currents and numerical dissipation of the diffusive part of advection scheme working at high frequencies. The location of the maxima of the vertical advection tendency at the shelf break and along the ITs propagation pathway and its negative sign, suggest that the diffusive part of the advection scheme might be the dominant process compared to nonlinear effects, as the velocity of the (mode-1) internal tidal waves is maximum in the thermocline where exactly z-ADV term is working harder.

V.2. On the role of advection in coastal upwelling

To explain the cooling of the SST at the surface, Neto and da Silva (2014) indicated that the steady flow of the NBC induces northward transport of water masses. This transport is in turn offset by a vertical advection of cool water towards the surface. We demonstrate with our

model that the vertical advection hardly modifies the SST. But it is rather working below the mixed layer (Fig.9e-h). The tides-induced vertical diffusion (mixing) extends from the mixed-layer to deeper layers (Fig.8e-f). It is therefore possible for the vertical mixing to bring up to the surface the water masses that are advected into the layers below the mixed layer. The change in SST and temperature within the mixed-layer can then be influence in first order by (i) the vertical diffusion of temperature and secondary by (ii) a cross effect between the latter and the advection (vertical and horizontal) of temperature that mainly takes place below the mixed-layer.

V.3. The mode-1 wave-like patterns in the vertical terms of the heat budget equation

Along the vertical and toward the open ocean, both ZDF and z-ADV tendencies are found to have a wave-like structure. For z-ADV, patches are spaced apart by about 120–150 km and 140–160 km for the AMJ and ASO seasons respectively. Whilst for z-ADV, this wavelength is about 140–160 km during the AMJ season and more continuous patches for the ASO season. The wavelength ranges found in temperature tendency terms (3T) are slightly wider (~ 10–20 km, for z-ADV in ASO season and for ZDF) than the purely dynamic tidal coherent wavelength (~ 120–150 km, see section III.1). The difference can be understood as the effect of incoherent ITs, i.e., ITs that are deviated or diffracted by the currents and/or eddies, for which dissipation occurs around where coherent ITs dissipate. They are uncaptured by the harmonic analysis. Hence, the total (coherent + incoherent) dissipation pattern of ITs could be wider than in Figure 2f. When integrating 3T over the season, this cumulative effect is considered and therefore leads to diffuse patterns and wider wavelength. This diffusive effect increases during the ASO season when both background circulation and eddy activity increase.

Recently, de Macedo et al. (2023) gave a detailed description of ISW in this region. They showed an intensification of ISW occurrences along A and B pathways, whose inter-packet distance corresponds to the wavelength of mode-1 ITs. These ISW packets are also colocalized (horizontally) with the deeper 3T patches. Our results are therefore consistent with the observations of the latter study regarding the localization of IT dissipation, particularly where they can generate ISW.

V.4. Tidal impact at the mouth of the Amazon River and on the southern shelf: two main competitive processes

Depending on the season, the mean SST anomaly [Tide – No-Tide] at the mouth of the Amazon and southeast of the plateau is either negative (AMJ, fig.5a) or positive (ASO, fig.5b). What we found can be explained by a combination of processes. Note that seasonal variations in solar radiation, river flow and stratification over the shelf can also play significant roles.

In the simulation without the tides, there is a strong coast-parallel current exiting northwesterly the mouth of the Amazon River (black arrows in Fig.11a, 11b; Ruault et al., 2020) with an average intensity > 0.5 $m.s^{-1}$ in the first 50 meters (color shading in Fig.11a, 11b). When including the tides in the model, the latter study had shown that there is an increase in the vertical mixing in the water column due to stratified-shear flow instability. They then show that this weakens the coast-parallel current and favors cross-shore export of water (color shading in Fig.11c, 11d), which is then diverted to the north-west (black arrows in Fig.11c, 11d). We can therefore establish that there are at least two processes at work in producing SST anomalies: (i) vertical mixing and (ii) horizontal transport, reflected respectively by ZDF and h-ADV. We then looked at the latter two processes along the vertical following the cross-shore transect (*C-S*) defined in Figure 10b. Hereinafter, inner mouth refers to the part of the transect before 200 km, whereas outer shelf refers to the part beyond.

During the AMJ season, in the inner mouth, river flow dominates and tide-induced vertical mixing in the narrow water column leads to warming and deepening of the thermocline (cyan and black lines in Fig.12a-b). On the outer shelf, this mixing in the thicker water column leads to cooling above the thermocline and warming below (Fig.12a). Which in turn extends across the shelf and along the pathways of ITs as shown in section IV.4.1 (see Fig.8a, 8c, and 8e-f). At the same time, the SST on the shelf is somewhat homogeneous (see Fig.4a-c) and solar radiation is lower than 190 $W.m^{-2}$ (not shown). As a result, waters of similar temperature are advected horizontally, i.e., the h-ADV is low (Fig.12b). Thus, for the first season, vertical mixing seems to be the dominant process explaining the average negative SST anomaly on the plateau.

For the second season, solar radiation on the shelf rose sharply with an average value of 60 $W.m^{-2}$ compared with the previous season (Fig.12c). The average depth of the thermocline deepens offshore (cyan and black lines Fig.12d and 12e). Here, mixing leads to warming in the thin surface layer (< 2m, Fig.12d). In contrast to AMJ, there is a significant horizontal variation in SST on the plateau (see Fig.4d-f). The NBC is stronger and can influence transport over the

shelf (Prestes et al., 2018). Even it is small, the mean tidal residual transport is added and should be taken into account (Bessières et al., 2008). Warm waters can therefore be advected across the shelf. Consequently, h-ADV is stronger and positive (Fig.12e) and plays a greater role in the fate of SST. For this season, ZDF and h-ADV add to explain the positive SST anomaly on the shelf.

From AMJ to ASO, we can note the deepening of the thermocline depth on the outer shelf. This was previously highlighted by Silva et al. (2005) from REVIZEE (Recursos Vivos da Zona Econômica Exclusiva) campaign data. This is a further contribution to the validation of our model in the section III.2.

V.5. Tidal impact in the NBC retroflection area

To the north-west of the domain [3°N–9°N and 53°W–45°W], in the surface layers (2–20m), eddy-like or circular patterns exist in ZDF during the ASO season for the simulation including tides (Fig.8c). It should be remembered that during this season the NBC intensifies and retroflects, and strong eddy activity takes place there. We therefore assume that they may be the driving force behind these ZDF patterns. However, it is not yet clear how these mesoscale features produce vertical mixing. They may be involved either by fronts or trapping the internal tidal waves.

1) **Fronts**: they exist in such a intensively active mesoscale region. They are associated with significant vertical mixing (see Chapman et al., 2020). We therefore looked at the horizontal temperature gradient (∇T) averaged over the same depth range (2–20m) as the ZDF (Fig.8a-d). During the AMJ season, it is on average equal to 4 10^{-2} °C/10 km. As expected, it does not reveal any circular fronts for the two simulations (Fig.13a-b) since mesoscale activity is low. Secondly, the horizontal gradient of the temperature increases during the ASO season [> 5 10^{-2} °C/10 km] in the north-west and exhibits circular and filamentary fronts in both the non-tidal (Fig.13c) and tidal (Fig.13d) simulations. Therefore, one would expect to see the same circular patterns in the ZDF for both simulations. This is not actually the case (see Fig.8c and 8d) and invalidates this statement. Furthermore, these values are at least three times smaller compared to other oceanic regions (e.g., Kostianoy et al., 2004 and Bouali et al., 2017), meaning that these fronts are less pronounced.
2) **Trapping internal tidal waves**: stronger mesoscale activity which occurs during this season implies more interaction between the background circulation and ITs (Buijsman

et al., 2017 and Tchilibou et al., 2022). The NBC flows along the coast and crosses the sites where ITs are generated (see schematic view in Fig.1). This means that ITs can be trapped and advected along the NBC pathway. When this current destabilizes and retroflects in the north-west, these trapped waves dissipate and therefore generate vertical mixing. This hits the high fraction of the incoherent ITs found here (Tchilibou et al., 2022). But quantifying the impact on temperature of such a wave-mean flow interaction process requires further analysis and is beyond the scope of this study.

Nevertheless, we believe that this second process could be the main cause of vertical diffusion of temperature in that region. Thus, from the section V.3 and the latter, we can conclude that incoherent ITs represent a significant part of the total energy of internal tides. But remains to be quantified in future work. In addition, in parallel with coherent ITs, they might play a critical role on the fate of the temperature in this region.

VI. Summary

In this paper, we used twin oceanic simulations (with and without tides) from a realistic model to explore the impact of internal tidal waves (ITs) on temperature and associated processes. The impact on the atmosphere-to-ocean net heat fluxes is also covered.

The AMAZON36 configuration can reproduce the generation of ITs from two most energetic sites A and B, in good agreement with previous studies. The model well reproduces the local, on-shelf, and offshore dissipation of ITs with two beams of mode-1 propagation (120–150 km). This dissipation occurs less than 300 km from the slope. Then, we assess the ability of the model to reproduce temperature structure. The simulations including tides is in better agreement with SST observations and better reproduce water mass properties along the vertical.

Our analyses were based on three years (2013 to 2015) data averaged over two seasons, AMJ (April-May-June) and ASO (August-September-October). That are highly contrasted in terms of stratification, background circulation and EKE. Results show that for both seasons, the tides create SST cooling of about 0.3 °C in the plume of the Amazon offshore and along the paths of propagation A and B of ITs. During ASO, the cold waters of the ACT enter our domain along the coast and are affected by the tides. This enhances that seasonal upwelling and leads to cooler SST. Over the Amazon shelf, the tides induce the same magnitude cooling in AMJ and in turn induce an opposite anomaly (warming) in ASO. These cooling/warming are responsible in the same location for an increase/decrease in the net heat flux from the atmosphere to the ocean (Qt). However, the overall effect of the tides is an increase of Qt, which

lies between [33.2% – 7.4%] from AMJ to ASO. And can be larger than what obtained elsewhere (e.g., in the Solomon Sea). In such a region with large atmospheric convection (marked by the ITCZ), when increasing the atmosphere-to-ocean net heat flux, the tides might reduce the cloud convection into the atmosphere (Koch-Larrouy et al., 2010). Therefore, this tidal effect on the climate might have a key importance for the future, taking the climate change into account (Yadidya and Rao, 2022).

In the subsurface, above the thermocline (< 120 m), the tides induce a stronger cooling (~1.2 °C) than at the surface. And an associated warming of the same magnitude under the thermocline (> 120–300 m). We analyzed the terms of the heat budget equation to identify to processes that modify the temperature. We found that the vertical diffusion of temperature (ZDF) is mainly caused by the dissipation of the tides. Horizontal (h-ADV) and vertical (z-ADV) advection can be driven by non-tidal processes but increase when including the tides in the model.

Over the shelf, barotropic tidal mixing increases ZDF (> |-0.4| °C.day^{-1}) and explain the cooling of the water column in AMJ season. During the second season, it combines with h-ADV and to cause a warming. Off the shelf, the (baroclinic) mixing takes place from the slope to about 700 km following the path A, and 300 km following the path B. That mixing induces ZDF with values of about -0.4 °C.day^{-1}, which is the main process in the upper layer above the mixed layer. But could combine with advection terms (z-ADV and h-ADV) to explain the temperature changes below the mixed layer. Along ITs propagation pathways, some ZDF and z-ADV patches follow the dissipation hotspots of the ITs, i.e., they exhibit the mode-1 propagation of ITs.

This study highlights the key role of ITs in creating intensified mixing which is important for temperature structure. Other analysis we performed with our simulations show that this mixing can also impacts salinity. Furthermore, they might be seen as a source of nutrient uptake at tidal frequency and can have an impact on the spatial distribution of phytoplankton and zooplankton, and therefore on the entire food chain (Sharples et al., 2007, 2009; Xu et al., 2020). These other impacts can be studied through a combined model-in situ data approach. A long-term PIRATA (PredIction and Research moored Array in the Tropical Atlantic) mooring data are available for this goal (Bourlès et al., 2019). In addition, recently in late 2021, the AMAZOn MIXing ("*AMAZOMIX*") campaign took place in this region. Among other things, this campaign was dedicated to ITs. It provided a huge set of data, with the aim of understanding their impact on marine ecosystems (see details in https://en.ird.fr/amazomix-

765 campaign-impact-physical-processes-marine-ecosystem-mouth-amazon). In the meantime, a
766 coupled physical/biogeochemistry simulation (NEMO/PISCES) is currently under analysis and
767 will begin to answer these crucial questions.
768 Finally, we focused hereabove on describing the impacts of tides on a seasonal scale. A
769 companion paper will then analyze the variability of temperature at tidal and subtidal scales
770 using our model simulations and two observational data.
771
772
773 ## Data availability
774 The TMI SST v7.1 data are publicly available online from the REMSS platform:
775 https://www.remss.com/missions/tmi/, was accessed on 27 June 2022. The model simulations
776 are available upon request by contacting the corresponding author.

777 ## Authors contributions
778 Funding acquisition, AKL; Conceptualization and methodology, FA, AKL and ID.
779 Numerical simulations, GM and FA. Formal analysis, FA; FA prepared the paper with
780 contribution from all co-authors.

781 ## Competing interests
782 The authors declare that they have no conflict of interest.
783

784 ## Funding
785 This work is part of the PhD Thesis of Fernand Assene, cofounded by Institut de
786 Recherche pour le Développement (IRD) and Mercator Ocean International (MOi), under the
787 cobadging of Ariane Koch-Larrouy and Isabelle Dadou. The numerical simulations were
788 founded by CNRS/CNES/IRD via the projects A0080111357 and A0130111357 and were
789 performed thank to "Jean-Zay", the CNRS/GENCI/IDRIS platform for modelling and
790 computing.

791 ## Acknowledgments
792 The authors would like to thank the Editorial team for their availability, and the two
793 reviewers Clément Vic and Nicolas Grissouard for their valuable comments, which enhanced
794 the quality of the present work. We also thank the NOAA Ocean Climate Laboratory for making
795 the WOA2018 products available.

References

Aguedjou, H.M.A., Dadou, I., Chaigneau, A., Morel, Y., Alory, G., 2019. Eddies in the Tropical Atlantic Ocean and Their Seasonal Variability. Geophys. Res. Lett. 46, 12156–12164. https://doi.org/10.1029/2019GL083925

Aguedjou, H.M.A., Chaigneau, A., Dadou, I., Morel, Y., Pegliasco, C., Da-Allada, C.Y., Baloïtcha, E., 2021. What Can We Learn From Observed Temperature and Salinity Isopycnal Anomalies at Eddy Generation Sites? Application in the Tropical Atlantic Ocean. J. Geophys. Res. Oceans 126, e2021JC017630. https://doi.org/10.1029/2021JC017630

Archer, D., Martin, P., Buffett, B., Brovkin, V., Rahmstorf, S., Ganopolski, A., 2004. The importance of ocean temperature to global biogeochemistry. Earth Planet. Sci. Lett. 222, 333–348. https://doi.org/10.1016/j.epsl.2004.03.011

Azevedo, A., da Silva, J.C.B., New, A.L., 2006. On the generation and propagation of internal solitary waves in the southern Bay of Biscay. Deep Sea Res. Part Oceanogr. Res. Pap. 53, 927–941. https://doi.org/10.1016/j.dsr.2006.01.013

Baines, P.G., 1982. On internal tide generation models. Deep Sea Res. Part Oceanogr. Res. Pap. 29, 307–338. https://doi.org/10.1016/0198-0149(82)90098-X

Barbot, S., Lyard, F., Tchilibou, M., Carrere, L., 2021. Background stratification impacts on internal tide generation and abyssal propagation in the western equatorial Atlantic and the Bay of Biscay. Ocean Sci. 17, 1563–1583. https://doi.org/10.5194/os-17-1563-2021

Barton, E.D., Inall, M.E., Sherwin, T.J., Torres, R., 2001. Vertical structure, turbulent mixing and fluxes during Lagrangian observations of an upwelling filament system off Northwest Iberia. Prog. Oceanogr., Lagrangian studies of the Iberian upwelling system 51, 249–267. https://doi.org/10.1016/S0079-6611(01)00069-6

Beardsley, R.C., Candela, J., Limeburner, R., Geyer, W.R., Lentz, S.J., Castro, B.M., Cacchione, D., Carneiro, N., 1995. The M2 tide on the Amazon Shelf. J. Geophys. Res. Oceans 100, 2283–2319. https://doi.org/10.1029/94JC01688

Bessières, L., 2007. Impact des marées sur la circulation générale océanique dans une perspective climatique (phdthesis). Université Paul Sabatier - Toulouse III.

Bessières, L., Madec, G., Lyard, F., 2008. Global tidal residual mean circulation: Does it affect a climate OGCM? Geophys. Res. Lett. 35. https://doi.org/10.1029/2007GL032644

Bouali, M., Sato, O.T., Polito, P.S., 2017. Temporal trends in sea surface temperature gradients in the South Atlantic Ocean. Remote Sens. Environ. 194, 100–114. https://doi.org/10.1016/j.rse.2017.03.008

Bourles, B., Molinari, R.L., Johns, E., Wilson, W.D., Leaman, K.D., 1999. Upper layer currents in the western tropical North Atlantic (1989–1991). J. Geophys. Res. Oceans 104, 1361–1375. https://doi.org/10.1029/1998JC900025

Bourlès, B., Araujo, M., McPhaden, M.J., Brandt, P., Foltz, G.R., Lumpkin, R., Giordani, H., Hernandez, F., Lefèvre, N., Nobre, P., Campos, E., Saravanan, R., Trotte-Duhà, J., Dengler, M., Hahn, J., Hummels, R., Lübbecke, J.F., Rouault, M., Cotrim, L., Sutton, A., Jochum, M., Perez, R.C., 2019. PIRATA: A Sustained Observing System for Tropical Atlantic Climate Research and Forecasting. Earth Space Sci. 6, 577–616. https://doi.org/10.1029/2018EA000428

Buijsman, M.C., Arbic, B.K., Richman, J.G., Shriver, J.F., Wallcraft, A.J., Zamudio, L., 2017. Semidiurnal internal tide incoherence in the equatorial Pacific. J. Geophys. Res. Oceans 122, 5286–5305. https://doi.org/10.1002/2016JC012590

C., Le Provost, Florent, Lyard, 1997. Energetics of the M2 barotropic ocean tides: an estimate of bottom friction dissipation from a hydrodynamic model - ScienceDirect. Prog. Oceanogr. 37–52.

Chapman, C.C., Lea, M.-A., Meyer, A., Sallée, J.-B., Hindell, M., 2020. Defining Southern Ocean fronts and their influence on biological and physical processes in a changing climate. Nat. Clim. Change 10, 209–219. https://doi.org/10.1038/s41558-020-0705-4

Clayson, C.A., Bogdanoff, A.S., 2013. The Effect of Diurnal Sea Surface Temperature Warming on Climatological Air–Sea Fluxes. J. Clim. 26, 2546–2556. https://doi.org/10.1175/JCLI-D-12-00062.1

Collins, M., An, S.-I., Cai, W., Ganachaud, A., Guilyardi, E., Jin, F.-F., Jochum, M., Lengaigne, M., Power, S., Timmermann, A., Vecchi, G., Wittenberg, A., 2010. The impact of global warming on the tropical Pacific Ocean and El Niño. Nat. Geosci. 3, 391–397. https://doi.org/10.1038/ngeo868

da Silva, J.C.B., New, A.L., Magalhaes, J.M., 2011. On the structure and propagation of internal solitary waves generated at the Mascarene Plateau in the Indian Ocean. Deep Sea Res. Part Oceanogr. Res. Pap. 58, 229–240. https://doi.org/10.1016/j.dsr.2010.12.003

de Lavergne, C., Vic, C., Madec, G., Roquet, F., Waterhouse, A.F., Whalen, C.B., Cuypers, Y., Bouruet-Aubertot, P., Ferron, B., Hibiya, T., 2020. A Parameterization of Local and Remote Tidal Mixing. J. Adv. Model. Earth Syst. 12, e2020MS002065. https://doi.org/10.1029/2020MS002065

de Macedo, C.R., Koch-Larrouy, A., da Silva, J.C.B., Magalhães, J.M., Lentini, C.A.D., Tran, T.K., Rosa, M.C.B., Vantrepotte, V., 2023. Spatial and temporal variability of mode-1 and mode-2 internal solitary waves from MODIS/TERRA sunglint off the Amazon shelf. EGUsphere 1–27. https://doi.org/10.5194/egusphere-2022-1482

Didden, N., Schott, F., 1993. Eddies in the North Brazil Current retroflection region observed by Geosat altimetry. J. Geophys. Res. Oceans 98, 20121–20131. https://doi.org/10.1029/93JC01184

Dong, S., Sprintall, J., Gille, S.T., Talley, L., 2008. Southern Ocean mixed-layer depth from Argo float profiles. J. Geophys. Res. Oceans 113. https://doi.org/10.1029/2006JC004051

873 Dunphy, M., Lamb, K.G., 2014. Focusing and vertical mode scattering of the first mode internal
874 tide by mesoscale eddy interaction. J. Geophys. Res. Oceans 119, 523–536.
875 https://doi.org/10.1002/2013JC009293

876 Egbert, G.D., Ray, R.D., 2000. Significant dissipation of tidal energy in the deep ocean inferred
877 from satellite altimeter data. Nature 405, 775–778. https://doi.org/10.1038/35015531

878 Fassoni-Andrade, A.C., Durand, F., Azevedo, A., Bertin, X., Santos, L.G., Khan, J.U., Testut,
879 L., Moreira, D.M., 2023. Seasonal to interannual variability of the tide in the Amazon
880 estuary. Cont. Shelf Res. 255, 104945. https://doi.org/10.1016/j.csr.2023.104945

881 Feng, Y., Tang, Q., Li, J., Sun, J., Zhan, W., 2021. Internal Solitary Waves Observed on the
882 Continental Shelf in the Northern South China Sea From Acoustic Backscatter Data.
883 Front. Mar. Sci. 8.

884 Fontes, R.F.C., Castro, B.M., Beardsley, R.C., 2008. Numerical study of circulation on the inner
885 Amazon Shelf. Ocean Dyn. 58, 187–198. https://doi.org/10.1007/s10236-008-0139-4

886 Gabioux, M., Vinzon, S.B., Paiva, A.M., 2005. Tidal propagation over fluid mud layers on the
887 Amazon shelf. Cont. Shelf Res. 25, 113–125. https://doi.org/10.1016/j.csr.2004.09.001

888 Garzoli, S.L., Ffield, A., Johns, W.E., Yao, Q., 2004. North Brazil Current retroflection and
889 transports. J. Geophys. Res. Oceans 109. https://doi.org/10.1029/2003JC001775

890 Gévaudan, M., Durand, F., Jouanno, J., 2022. Influence of the Amazon-Orinoco Discharge
891 Interannual Variability on the Western Tropical Atlantic Salinity and Temperature. J.
892 Geophys. Res. Oceans 127, e2022JC018495. https://doi.org/10.1029/2022JC018495

893 Hernandez, O., Jouanno, J., Durand, F., 2016. Do the Amazon and Orinoco freshwater plumes
894 really matter for hurricane-induced ocean surface cooling? J. Geophys. Res. Oceans
895 121, 2119–2141. https://doi.org/10.1002/2015JC011021

896 Hernandez, O., Jouanno, J., Echevin, V., Aumont, O., 2017. Modification of sea surface
897 temperature by chlorophyll concentration in the Atlantic upwelling systems. J. Geophys.
898 Res. Oceans 122, 5367–5389. https://doi.org/10.1002/2016JC012330

899 Hersbach, H., Bell, B., Berrisford, P., Hirahara, S., Horányi, A., Muñoz-Sabater, J., Nicolas, J.,
900 Peubey, C., Radu, R., Schepers, D., Simmons, A., Soci, C., Abdalla, S., Abellan, X.,
901 Balsamo, G., Bechtold, P., Biavati, G., Bidlot, J., Bonavita, M., De Chiara, G.,
902 Dahlgren, P., Dee, D., Diamantakis, M., Dragani, R., Flemming, J., Forbes, R., Fuentes,
903 M., Geer, A., Haimberger, L., Healy, S., Hogan, R.J., Hólm, E., Janisková, M., Keeley,
904 S., Laloyaux, P., Lopez, P., Lupu, C., Radnoti, G., de Rosnay, P., Rozum, I., Vamborg,
905 F., Villaume, S., Thépaut, J.-N., 2020. The ERA5 global reanalysis. Q. J. R. Meteorol.
906 Soc. 146, 1999–2049. https://doi.org/10.1002/qj.3803

907 HYBAM (2018) Contrôles géodynamique, hydrologique et biogéochimique de
908 l'érosion/altération et des transferts de matière dans les bassins de l'Amazone, de
909 l'Orénoque et du Congo. http://www.ore-hybam.org. Accessed 10 December 2021

910 Jayakrishnan, P.R., Babu, C.A., 2013. Study of the Oceanic Heat Budget Components over the
911 Arabian Sea during the Formation and Evolution of Super Cyclone, Gonu 2013.
912 https://doi.org/10.4236/acs.2013.33030

913 Jithin, A.K., Francis, P.A., 2020. Role of internal tide mixing in keeping the deep Andaman Sea
914 warmer than the Bay of Bengal. Sci. Rep. 10, 11982. https://doi.org/10.1038/s41598-
915 020-68708-6

916 Johns, W.E., Lee, T.N., Beardsley, R.C., Candela, J., Limeburner, R., Castro, B., 1998. Annual
917 Cycle and Variability of the North Brazil Current. J. Phys. Oceanogr. 28, 103–128.
918 https://doi.org/10.1175/1520-0485(1998)028<0103:ACAVOT>2.0.CO;2

919 Jouanno, J., Marin, F., du Penhoat, Y., Sheinbaum, J., Molines, J.-M., 2011. Seasonal heat
920 balance in the upper 100 m of the equatorial Atlantic Ocean. J. Geophys. Res. Oceans
921 116. https://doi.org/10.1029/2010JC006912

922 Kara, A.B., Rochford, P.A., Hurlburt, H.E., 2003. Mixed layer depth variability over the global
923 ocean. J. Geophys. Res. Oceans 108. https://doi.org/10.1029/2000JC000736

924 Kelly, S.M., Nash, J.D., Kunze, E., 2010. Internal-tide energy over topography. J. Geophys.
925 Res. Oceans 115. https://doi.org/10.1029/2009JC005618

926 Koch-Larrouy, A., Madec, G., Bouruet-Aubertot, P., Gerkema, T., Bessières, L., Molcard, R.,
927 2007. On the transformation of Pacific Water into Indonesian Throughflow Water by
928 internal tidal mixing. Geophys. Res. Lett. 34. https://doi.org/10.1029/2006GL028405

929 Koch-Larrouy, A., Madec, G., Iudicone, D., Atmadipoera, A., Molcard, R., 2008. Physical
930 processes contributing to the water mass transformation of the Indonesian Throughflow.
931 Ocean Dyn. 58, 275–288. https://doi.org/10.1007/s10236-008-0154-5

932 Koch-Larrouy, A., Lengaigne, M., Terray, P., Madec, G., Masson, S., 2010. Tidal mixing in the
933 Indonesian Seas and its effect on the tropical climate system. Clim. Dyn. 34, 891–904.
934 https://doi.org/10.1007/s00382-009-0642-4

935 Koch-Larrouy, A., Atmadipoera, A., van Beek, P., Madec, G., Aucan, J., Lyard, F., Grelet, J.,
936 Souhaut, M., 2015. Estimates of tidal mixing in the Indonesian archipelago from
937 multidisciplinary INDOMIX in-situ data. Deep Sea Res. Part Oceanogr. Res. Pap. 106,
938 136–153. https://doi.org/10.1016/j.dsr.2015.09.007

939 Kostianoy, A.G., Ginzburg, A.I., Frankignoulle, M., Delille, B., 2004. Fronts in the Southern
940 Indian Ocean as inferred from satellite sea surface temperature data. J. Mar. Syst. 45,
941 55–73. https://doi.org/10.1016/j.jmarsys.2003.09.004

942 Kosuth, P., Callède, J., Laraque, A., Filizola, N., Guyot, J.L., Seyler, P., Fritsch, J.M.,
943 Guimarães, V., 2009. Sea-tide effects on flows in the lower reaches of the Amazon
944 River. Hydrol. Process. 23, 3141–3150. https://doi.org/10.1002/hyp.7387

945 Kunze, E., MacKay, C., McPhee-Shaw, E.E., Morrice, K., Girton, J.B., Terker, S.R., 2012.
946 Turbulent Mixing and Exchange with Interior Waters on Sloping Boundaries. J. Phys.
947 Oceanogr. 42, 910–927. https://doi.org/10.1175/JPO-D-11-075.1

948 Lambeck, K., Runcorn, S.K., 1977. Tidal dissipation in the oceans: astronomical, geophysical
949 and oceanographic consequences. Philos. Trans. R. Soc. Lond. Ser. Math. Phys. Sci.
950 287, 545–594. https://doi.org/10.1098/rsta.1977.0159

951 Lascaratos, A., 1993. Estimation of deep and intermediate water mass formation rates in the
952 Mediterranean Sea. Deep Sea Res. Part II Top. Stud. Oceanogr. 40, 1327–1332.
953 https://doi.org/10.1016/0967-0645(93)90072-U

954 Laurent, L.S., Garrett, C., 2002. The Role of Internal Tides in Mixing the Deep Ocean. J. Phys.
955 Oceanogr. 32, 2882–2899. https://doi.org/10.1175/1520-
956 0485(2002)032<2882:TROITI>2.0.CO;2

957 Leclair, M., Madec, G., 2009. A conservative leapfrog time stepping method. Ocean Model.
958 30, 88–94. https://doi.org/10.1016/j.ocemod.2009.06.006

959 Lellouche, J.-M., Greiner, E., Le Galloudec, O., Garric, G., Regnier, C., Drevillon, M.,
960 Benkiran, M., Testut, C.-E., Bourdalle-Badie, R., Gasparin, F., Hernandez, O., Levier,
961 B., Drillet, Y., Remy, E., Le Traon, P.-Y., 2018. Recent updates to the Copernicus
962 Marine Service global ocean monitoring and forecasting real-time 1⁄12° high-resolution
963 system. Ocean Sci. 14, 1093–1126. https://doi.org/10.5194/os-14-1093-2018

964 Lentini, C.A.D., Magalhães, J.M., da Silva, J.C.B., Lorenzzetti, J.A., 2016. Transcritical Flow
965 and Generation of Internal Solitary Waves off the Amazon River: Synthetic Aperture
966 Radar Observations and Interpretation. Oceanography 29, 187–195.

967 Lentz, S.J., Limeburner, R., 1995. The Amazon River Plume during AMASSEDS: Spatial
968 characteristics and salinity variability. J. Geophys. Res. Oceans 100, 2355–2375.
969 https://doi.org/10.1029/94JC01411

970 Li, C., Zhou, W., Jia, X., Wang, X., 2006. Decadal/interdecadal variations of the ocean
971 temperature and its impacts on climate. Adv. Atmospheric Sci. 23, 964–981.
972 https://doi.org/10.1007/s00376-006-0964-7

973 Li, Y., Curchitser, E.N., Wang, J., Peng, S., 2020. Tidal Effects on the Surface Water Cooling
974 Northeast of Hainan Island, South China Sea. J. Geophys. Res. Oceans 125,
975 e2019JC016016. https://doi.org/10.1029/2019JC016016

976 Lyard, F.H., Allain, D.J., Cancet, M., Carrère, L., Picot, N., 2021. FES2014 global ocean tide
977 atlas: design and performance. Ocean Sci. 17, 615–649. https://doi.org/10.5194/os-17-
978 615-2021

979 Madec, G., Bourdallé-Badie, R., Chanut, J., Clementi, E., Coward, A., Ethé, C., Iovino, D., Lea,
980 D., Lévy, C., Lovato, T., Martin, N., Masson, S., Mocavero, S., Rousset, C., Storkey,
981 D., Vancoppenolle, M., Müeller, S., Nurser, G., Bell, M., & Samson, G., (2019). NEMO
982 ocean engine. In Notes du Pôle de modélisation de l'Institut Pierre-Simon Laplace
983 (IPSL) (v4.0, Number 27). Zenodo. https://doi.org/10.5281/zenodo.3878122

984 Magalhaes, J.M., da Silva, J.C.B., Buijsman, M.C., Garcia, C. a. E., 2016. Effect of the North
985 Equatorial Counter Current on the generation and propagation of internal solitary waves
986 off the Amazon shelf (SAR observations). Ocean Sci. 12, 243–255.
987 https://doi.org/10.5194/os-12-243-2016

Mei, W., Xie, S.-P., Primeau, F., McWilliams, J.C., Pasquero, C., 2015. Northwestern Pacific typhoon intensity controlled by changes in ocean temperatures. Sci. Adv. 1, e1500014. https://doi.org/10.1126/sciadv.1500014

Moisan, J.R., Niiler, P.P., 1998. The Seasonal Heat Budget of the North Pacific: Net Heat Flux and Heat Storage Rates (1950–1990). J. Phys. Oceanogr. 28, 401–421. https://doi.org/10.1175/1520-0485(1998)028<0401:TSHBOT>2.0.CO;2

Muller-Karger, F.E., McClain, C.R., Richardson, P.L., 1988. The dispersal of the Amazon's water. Nature 333, 56–59. https://doi.org/10.1038/333056a0

Munk, W., Wunsch, C., 1998. Abyssal recipes II: energetics of tidal and wind mixing. Deep Sea Res. Part Oceanogr. Res. Pap. 45, 1977–2010. https://doi.org/10.1016/S0967-0637(98)00070-3

Nagai, T., Hibiya, T., 2015. Internal tides and associated vertical mixing in the Indonesian Archipelago. J. Geophys. Res. Oceans 120, 3373–3390. https://doi.org/10.1002/2014JC010592

Nash, J.D., Alford, M.H., Kunze, E., Martini, K., Kelly, S., 2007. Hotspots of deep ocean mixing on the Oregon continental slope. Geophys. Res. Lett. 34. https://doi.org/10.1029/2006GL028170

Neto, A.V.N., da Silva, A.C., 2014. Seawater temperature changes associated with the North Brazil current dynamics. Ocean Dyn. 64, 13–27. https://doi.org/10.1007/s10236-013-0667-4

New, A.L., Pingree, R.D., 2000. An intercomparison of internal solitary waves in the Bay of Biscay and resulting from Korteweg-de Vries-Type theory. Prog. Oceanogr. 45, 1–38. https://doi.org/10.1016/S0079-6611(99)00049-X

New, A.L., Pingree, R.D., 1990. Large-amplitude internal soliton packets in the central Bay of Biscay. Deep Sea Res. Part Oceanogr. Res. Pap. 37, 513–524. https://doi.org/10.1016/0198-0149(90)90022-N

Niwa, Y., Hibiya, T., 2011. Estimation of baroclinic tide energy available for deep ocean mixing based on three-dimensional global numerical simulations. J. Oceanogr. 67, 493–502. https://doi.org/10.1007/s10872-011-0052-1

Nugroho, D., Koch-Larrouy, A., Gaspar, P., Lyard, F., Reffray, G., Tranchant, B., 2018. Modelling explicit tides in the Indonesian seas: An important process for surface sea water properties. Mar. Pollut. Bull., Special Issue: Indonesia seas management 131, 7–18. https://doi.org/10.1016/j.marpolbul.2017.06.033

Peng, S., Liao, J., Wang, X., Liu, Z., Liu, Y., Zhu, Y., Li, B., Khokiattiwong, S., Yu, W., 2021. Energetics Based Estimation of the Diapycnal Mixing Induced by Internal Tides in the Andaman Sea. J. Geophys. Res. Oceans 126. https://doi.org/10.1029/2020JC016521

Prestes, Y.O., Silva, A.C. da, Jeandel, C., 2018. Amazon water lenses and the influence of the North Brazil Current on the continental shelf. Cont. Shelf Res. 160, 36–48. https://doi.org/10.1016/j.csr.2018.04.002

Purwandana, A., Cuypers, Y., Bourgault, D., Bouruet-Aubertot, P., Santoso, P.D., 2022. Fate of internal solitary wave and enhanced mixing in Manado Bay, North Sulawesi, Indonesia. Cont. Shelf Res. 245, 104801. https://doi.org/10.1016/j.csr.2022.104801

Richardson, P.L., Hufford, G.E., Limeburner, R., Brown, W.S., 1994. North Brazil Current retroflection eddies. J. Geophys. Res. Oceans 99, 5081–5093. https://doi.org/10.1029/93JC03486

Rosenthal, Y., Boyle, E.A., Slowey, N., 1997. Temperature control on the incorporation of magnesium, strontium, fluorine, and cadmium into benthic foraminiferal shells from Little Bahama Bank: Prospects for thermocline paleoceanography. Geochim. Cosmochim. Acta 61, 3633–3643. https://doi.org/10.1016/S0016-7037(97)00181-6

Ruault, V., Jouanno, J., Durand, F., Chanut, J., Benshila, R., 2020. Role of the Tide on the Structure of the Amazon Plume: A Numerical Modeling Approach. J. Geophys. Res. Oceans 125, e2019JC015495. https://doi.org/10.1029/2019JC015495

Salamena, G.G., Whinney, J.C., Heron, S.F., Ridd, P.V., 2021. Internal tidal waves and deep-water renewal in a tropical fjord: Lessons from Ambon Bay, eastern Indonesia. Estuar. Coast. Shelf Sci. 253, 107291. https://doi.org/10.1016/j.ecss.2021.107291

Sandstrom, H., Oakey, N.S., 1995. Dissipation in Internal Tides and Solitary Waves. J. Phys. Oceanogr. 25, 604–614. https://doi.org/10.1175/1520-0485(1995)025<0604:DIITAS>2.0.CO;2

Schott, F.A., Dengler, M., Brandt, P., Affler, K., Fischer, J., Bourlès, B., Gouriou, Y., Molinari, R.L., Rhein, M., 2003. The zonal currents and transports at 35°W in the tropical Atlantic. Geophys. Res. Lett. 30. https://doi.org/10.1029/2002GL016849

Sharples, J., Moore, C.M., Hickman, A.E., Holligan, P.M., Tweddle, J.F., Palmer, M.R., Simpson, J.H., 2009. Internal tidal mixing as a control on continental margin ecosystems. Geophys. Res. Lett. 36. https://doi.org/10.1029/2009GL040683

Sharples, J., Tweddle, J.F., Green, J.A.M., Palmer, M.R., Kim, Y.-N., Hickman, A.E., Holligan, P.M., Moore, C.M., Rippeth, T.P., Simpson, J.H., Krivtsov, V., 2007. Spring-neap modulation of internal tide mixing and vertical nitrate fluxes at a shelf edge in summer. Limnol. Oceanogr. 52, 1735–1747. https://doi.org/10.4319/lo.2007.52.5.1735

Silva, A., Araujo, M., Medeiros, C., Silva, M., Bourles, B., 2005. Seasonal changes in the mixed and barrier layers in the western Equatorial Atlantic. Braz. J. Oceanogr. 53, 83–98.

Smith, K.A., Rocheleau, G., Merrifield, M.A., Jaramillo, S., Pawlak, G., 2016. Temperature variability caused by internal tides in the coral reef ecosystem of Hanauma bay, Hawai‘i. Cont. Shelf Res. 116, 1–12. https://doi.org/10.1016/j.csr.2016.01.004

Speer, K.G., Isemer, H.-J., Biastoch, A., 1995. Water mass formation from revised COADS data. J. Phys. Oceanogr. 25, 2444–2457.

Sprintall, J., Gordon, A.L., Koch-Larrouy, A., Lee, T., Potemra, J.T., Pujiana, K., Wijffels, S.E., 2014. The Indonesian seas and their role in the coupled ocean–climate system. Nat. Geosci. 7, 487–492. https://doi.org/10.1038/ngeo2188

1066 Sprintall, J., Gordon, A.L., Wijffels, S.E., Feng, M., Hu, S., Koch-Larrouy, A., Phillips, H.,
1067 Nugroho, D., Napitu, A., Pujiana, K., Susanto, R.D., Sloyan, B., Peña-Molino, B., Yuan,
1068 D., Riama, N.F., Siswanto, S., Kuswardani, A., Arifin, Z., Wahyudi, A.J., Zhou, H.,
1069 Nagai, T., Ansong, J.K., Bourdalle-Badié, R., Chanut, J., Lyard, F., Arbic, B.K.,
1070 Ramdhani, A., Setiawan, A., 2019. Detecting Change in the Indonesian Seas. Front.
1071 Mar. Sci. 6.

1072 Swift, J.H., Aagaard, K., 1981. Seasonal transitions and water mass formation in the Iceland
1073 and Greenland seas. Deep Sea Res. Part Oceanogr. Res. Pap. 28, 1107–1129.
1074 https://doi.org/10.1016/0198-0149(81)90050-9

1075 Tchilibou, M., Gourdeau, L., Lyard, F., Morrow, R., Koch Larrouy, A., Allain, D., Djath, B.,
1076 2020. Internal tides in the Solomon Sea in contrasted ENSO conditions. Ocean Sci. 16,
1077 615–635. https://doi.org/10.5194/os-16-615-2020

1078 Tchilibou, M., Gourdeau, L., Morrow, R., Serazin, G., Djath, B., Lyard, F., 2018. Spectral
1079 signatures of the tropical Pacific dynamics from model and altimetry: a focus on the
1080 meso-/submesoscale range. Ocean Sci. 14, 1283–1301. https://doi.org/10.5194/os-14-
1081 1283-2018

1082 Tchilibou, M., Koch-Larrouy, A., Barbot, S., Lyard, F., Morel, Y., Jouanno, J., Morrow, R.,
1083 2022. Internal tides off the Amazon shelf during two contrasted seasons: interactions
1084 with background circulation and SSH imprints. Ocean Sci. 18, 1591–1618.
1085 https://doi.org/10.5194/os-18-1591-2022

1086 Varona, H.L., Veleda, D., Silva, M., Cintra, M., Araujo, M., 2019. Amazon River plume
1087 influence on Western Tropical Atlantic dynamic variability. Dyn. Atmospheres Oceans
1088 85, 1–15. https://doi.org/10.1016/j.dynatmoce.2018.10.002

1089 Vic, C., Naveira Garabato, A.C., Green, J.A.M., Waterhouse, A.F., Zhao, Z., Melet, A., de
1090 Lavergne, C., Buijsman, M.C., Stephenson, G.R., 2019. Deep-ocean mixing driven by
1091 small-scale internal tides. Nat. Commun. 10, 2099. https://doi.org/10.1038/s41467-019-
1092 10149-5

1093 Vlasenko, V., Stashchuk, N., 2006. Amplification and Suppression of Internal Waves by Tides
1094 over Variable Bottom Topography. J. Phys. Oceanogr. 36, 1959–1973.
1095 https://doi.org/10.1175/JPO2958.1

1096 Wallace, M.I., Meredith, M.P., Brandon, M.A., Sherwin, T.J., Dale, A., Clarke, A., 2008. On
1097 the characteristics of internal tides and coastal upwelling behaviour in Marguerite Bay,
1098 west Antarctic Peninsula. Deep Sea Res. Part II Top. Stud. Oceanogr. 55, 2023–2040.
1099 https://doi.org/10.1016/j.dsr2.2008.04.033

1100 Wang, X., Peng, S., Liu, Z., Huang, R.X., Qian, Y.-K., Li, Y., 2016. Tidal Mixing in the South
1101 China Sea: An Estimate Based on the Internal Tide Energetics. J. Phys. Oceanogr. 46,
1102 107–124. https://doi.org/10.1175/JPO-D-15-0082.1

1103 Wentz, F.J., C. Gentemann, K.A. Hilburn, 2015: Remote Sensing Systems TRMM TMI [Daily]
1104 Environmental Suite on 0.25 deg grid, Version 7.1. Remote Sensing Systems, Santa
1105 Rosa, CA. Available online at www.remss.com/missions/tmi.

Whalen, C.B., de Lavergne, C., Naveira Garabato, A.C., Klymak, J.M., MacKinnon, J.A., Sheen, K.L., 2020. Internal wave-driven mixing: governing processes and consequences for climate. Nat. Rev. Earth Environ. 1, 606–621. https://doi.org/10.1038/s43017-020-0097-z

Xie, S.-P., Carton, J.A., 2004. Tropical Atlantic variability: Patterns, mechanisms, and impacts. Wash. DC Am. Geophys. Union Geophys. Monogr. Ser. 147, 121–142. https://doi.org/10.1029/147GM07

Xu, P., Yang, W., Zhu, B., Wei, H., Zhao, L., Nie, H., 2020. Turbulent mixing and vertical nitrate flux induced by the semidiurnal internal tides in the southern Yellow Sea. Cont. Shelf Res. 208, 104240. https://doi.org/10.1016/j.csr.2020.104240

Yadidya, B., Rao, A.D., 2022. Projected climate variability of internal waves in the Andaman Sea. Commun. Earth Environ. 3, 1–12. https://doi.org/10.1038/s43247-022-00574-8

Zalesak, S.T., 1979. Fully multidimensional flux-corrected transport algorithms for fluids. J. Comput. Phys. 31, 335–362. https://doi.org/10.1016/0021-9991(79)90051-2

Zaron, E.D., 2017. Mapping the nonstationary internal tide with satellite altimetry. J. Geophys. Res. Oceans 122, 539–554. https://doi.org/10.1002/2016JC012487

Zaron, E.D., 2019. Baroclinic Tidal Sea Level from Exact-Repeat Mission Altimetry. J. Phys. Oceanogr. 49, 193–210. https://doi.org/10.1175/JPO-D-18-0127.1

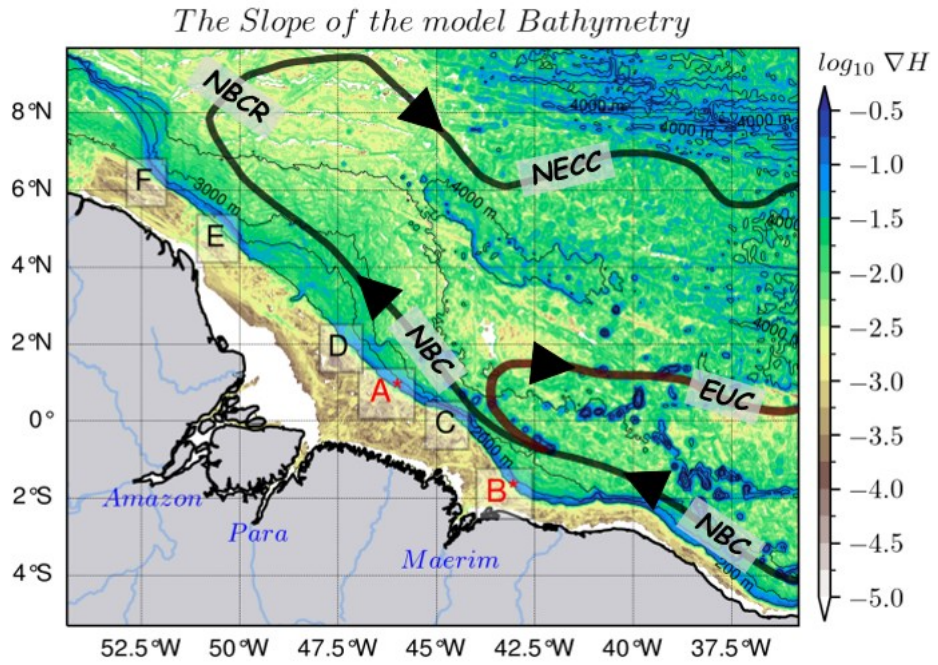

Figure 1: The horizontal gradient (∇H) of the model's bathymetry with different internal tides generation sites (A, B*, C, D, E and F) along the high slope (blue color shading) of the shelf break, with the two main sites A* and B* (in red), as reported in Magalhaes et al. (2016) and Tchilibou et al. (2022). Solid bold lines represent a schematic view of the circulation (as described by Didden and Schott, 1993; Richardson et al., 1994; Johns et al., 1998; Bourles et al., 1999a; Schott et al., 2003; Garzoli et al., 2004) with NBC, NBCR and NECC tracks in black, and the EUC track in brown red. Tin black contours are 200 m, 2000 m, 3000 m and 4000 m isobaths.*

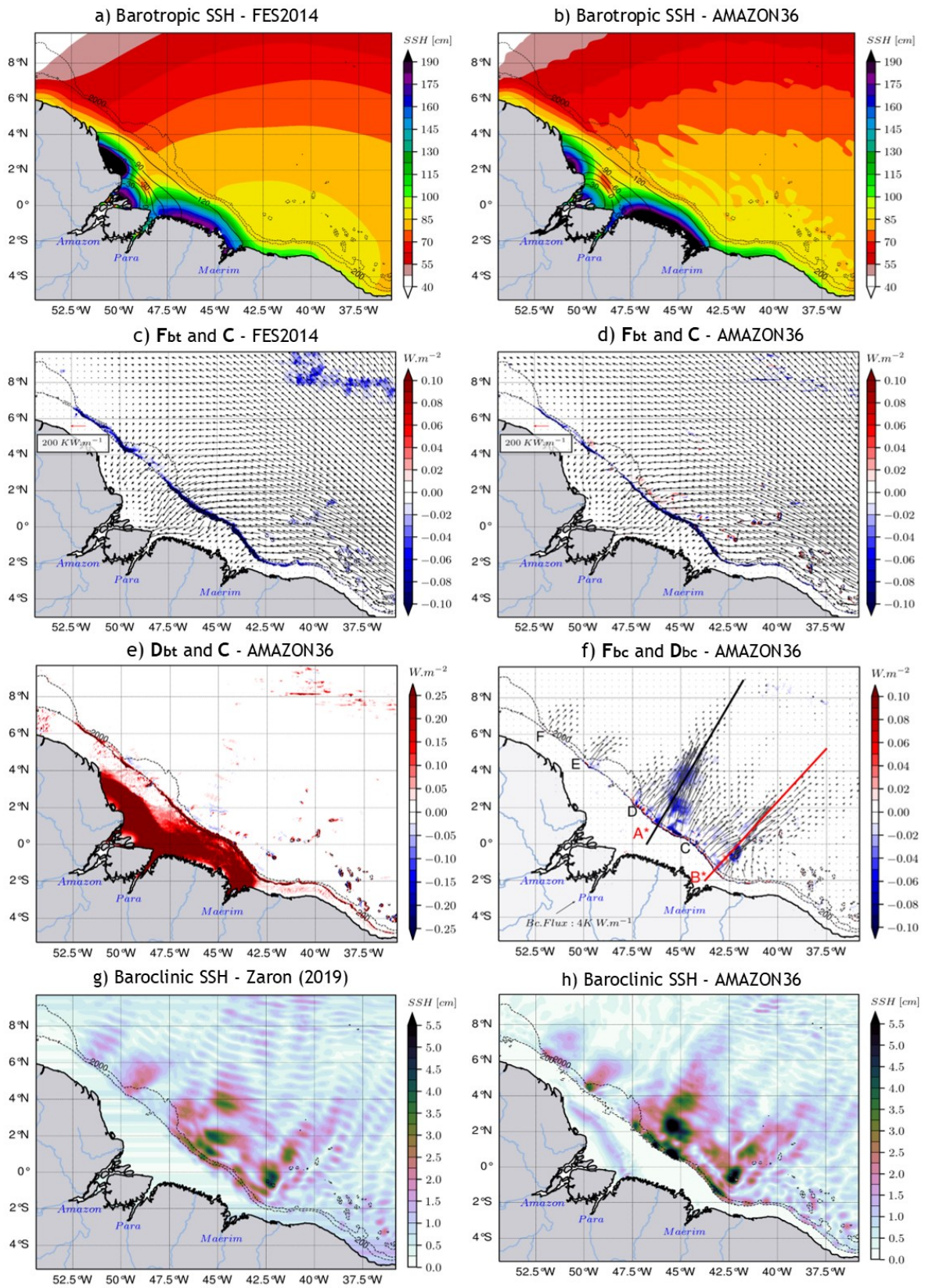

bt : barotropic ; **bc** : baroclinic

F : energy flux ; **C** : barotropic-to-baroclinic energy conversion ; **D** : energy dissipation

1138

Figure 2: Coherent (or stationary) characteristics of the M2 tides. Barotropic sea surface height (color shading) and its phase (solid tin contours) for (a) FES2014 and (b) the model, barotropic energy flux (black arrows) with the energy conversion rate (color shading) for (c) FES2014 and (d) the model, (e) the model depth-integrated barotropic energy dissipation, (f) the model depth-integrated baroclinic energy flux (black arrows) and the depth-integrated baroclinic energy dissipation (color shading) with transect lines along ITs trajectories A (black) and B* (red), the baroclinic sea surface height from (g) Zaron (2019) and (h) the model. Data from the model are the mean value over the year 2015. For all panels, dashed black lines represent the 200 m and 2000 m isobaths of the model bathymetry.*

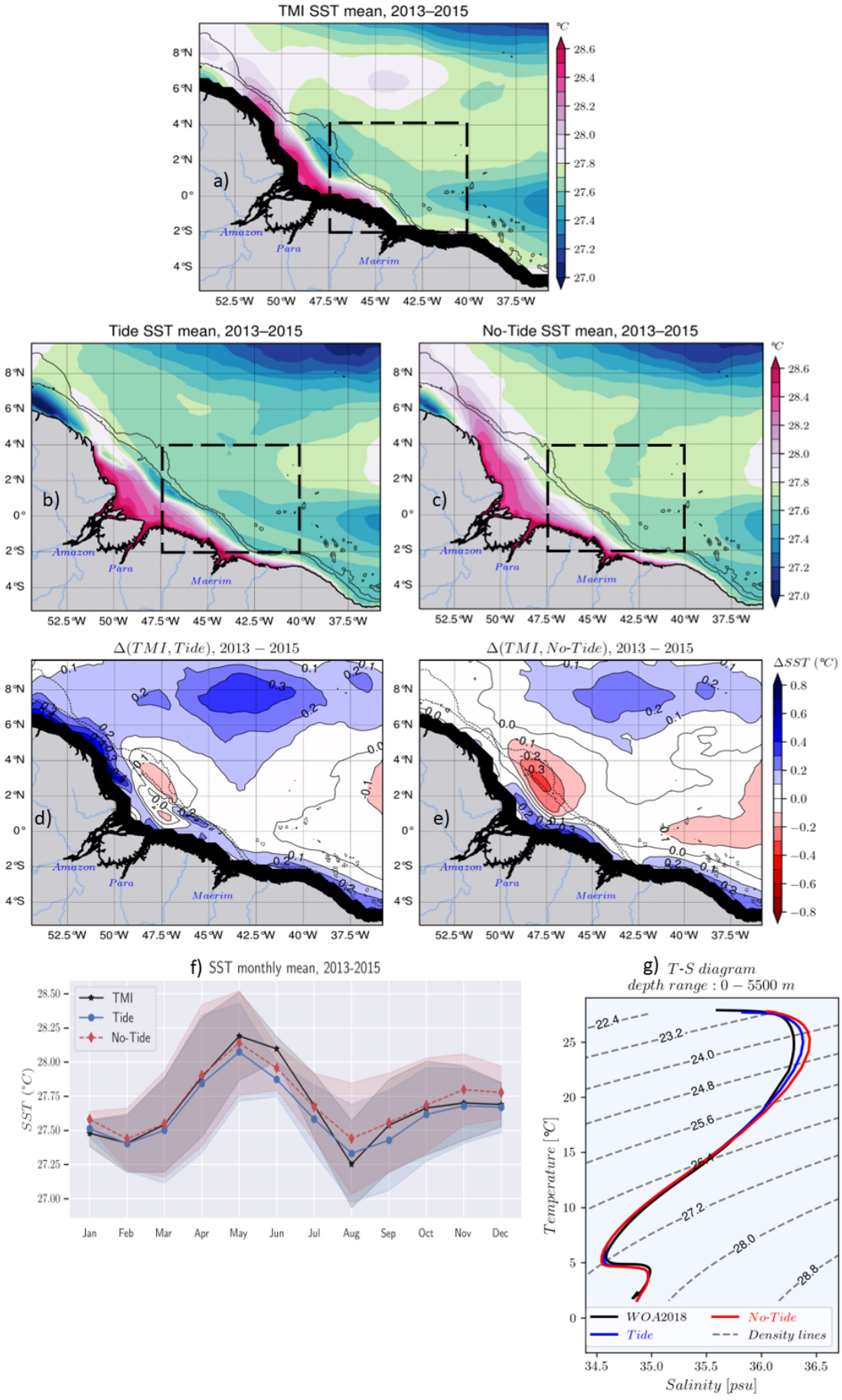
TMI SST mean, 2013–2015
Tide SST mean, 2013–2015
No-Tide SST mean, 2013–2015
$\Delta(TMI, Tide)$, 2013 – 2015
$\Delta(TMI, No\text{-}Tide)$, 2013 – 2015
ΔSST (°C)
a)
b)
c)
d)
e)
Amazon
Para
Maerim
f) SST monthly mean, 2013-2015
TMI
Tide
No-Tide
SST (°C)
Jan
Feb
Mar
Apr
May
Jun
Jul
Aug
Sep
Oct
Nov
Dec
g) T-S diagram
depth range : 0 – 5500 m
Temperature [°C]
Salinity [psu]
WOA2018
Tide
No-Tide
Density lines

Figure 3: Validation of the model temperature for the whole period 2013-2015. Mean SST for (a) TMI with its black coastal mask, (b) the tidal simulation, (c) the non-tidal simulation, the difference (bias) in SST between TMI and (d) the tidal simulation and (e) the non-tidal simulation, (f) the seasonal cycle of the SST of the three products averaged within the dashed line box in upper panels (covering ITs pathways emanating from the main generation sites A and B) with values masked below the 200 m isobath, bands indiciate variability according to standard deviation, (g) Temperature-Salinity (T-S) diagram of the mean properties in the same area as (e) from observed WOA2018 climatology (black line), the tidal simulation (blue line) and non-tidal simulation (red line) for the water column from surface to 5500 m depth, dashed gray lines represent density (σ_θ) contours. For panels a-e and hereinafter (unless otherwise stated), the solid black lines represent the 200 m and 2000 m isobaths from the model bathymetry.

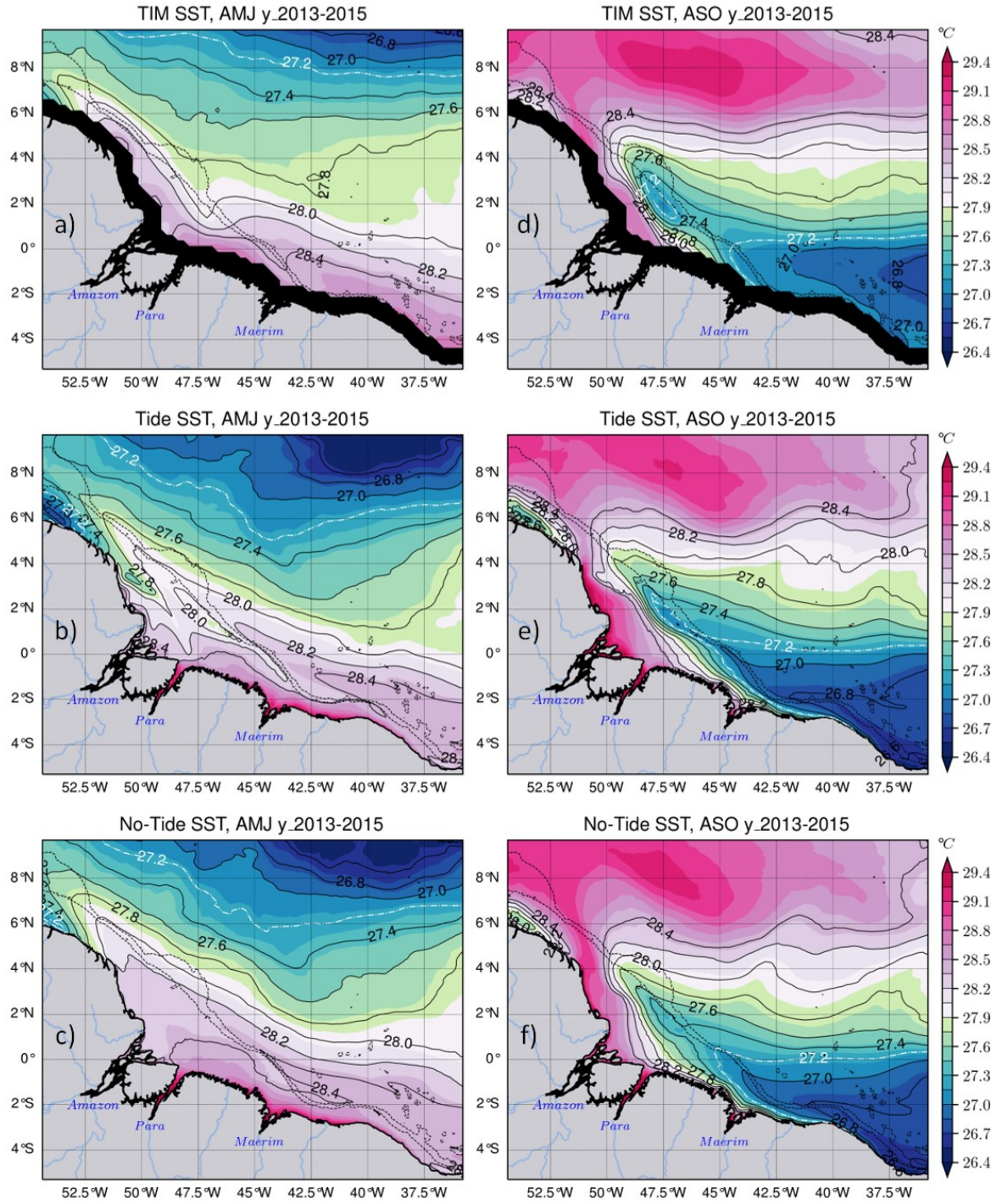

Figure 4: 2013-2015 seasonal SST mean. The left panels stand for the AMJ season for TMI with its black coastal mask, the tidal simulation and the non-tidal simulation, respectively for the upper-left, center-left and lower-left panel; the same in the panels on the right but for the ASO season. The dashed white and black solid lines represent the temperature contours. Dashed black lines stand for the 200 m and 2000 m isobaths from the model bathymetry.

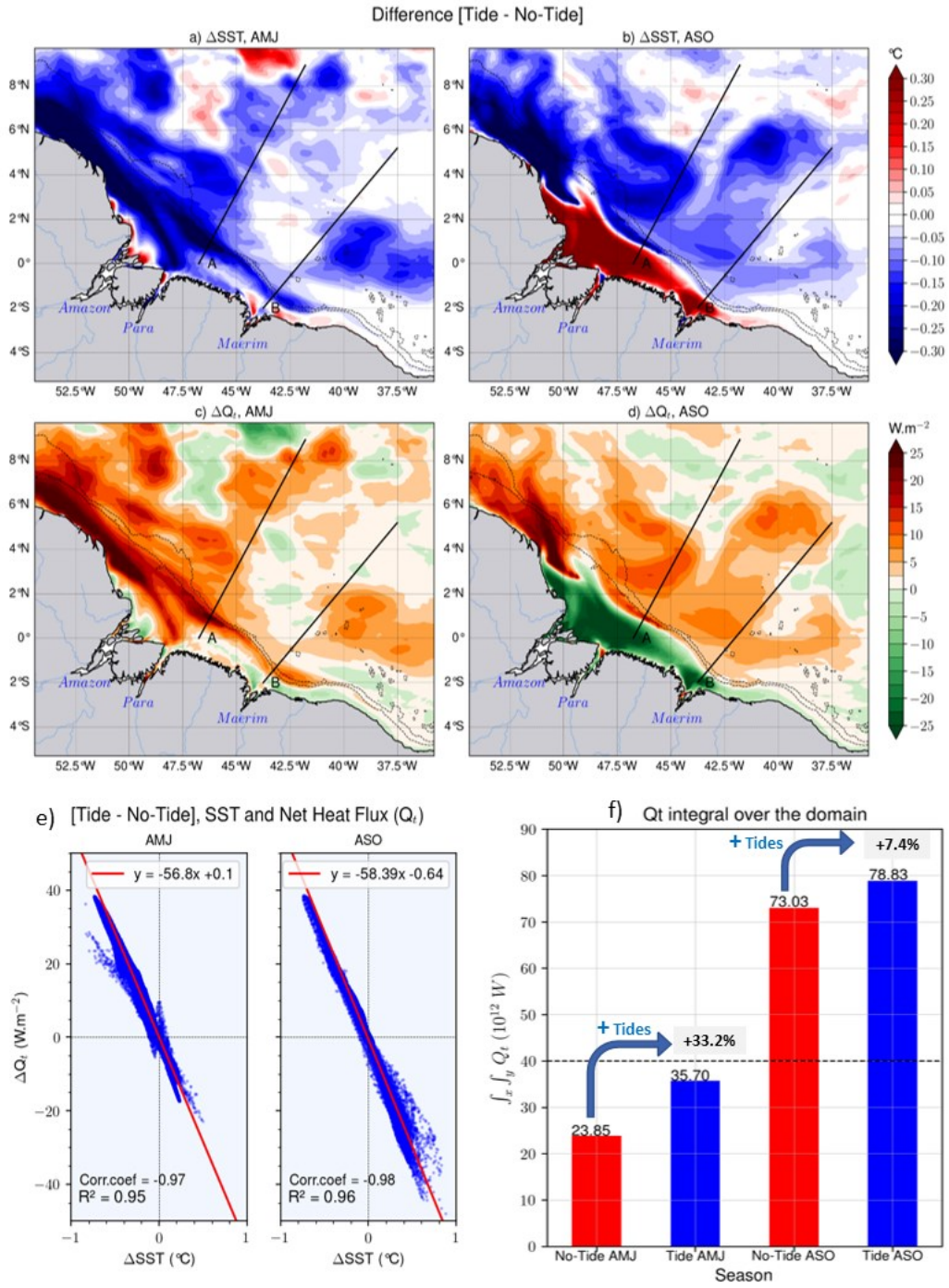

Figure 5: Relationship between the SST and the atmosphere-to-ocean net heat flux (Qt): SST anomaly [Tide - No-Tide] in AMJ (a) and ASO (b) seasons, Qt anomaly in AMJ (c) and ASO (d) seasons, (e) correlation between Qt anomaly and SST anomaly for each season, (f) domain integrated Qt for both seasons of each simulation. Hereinafter, -anomaly- refers to what is described hereabove.

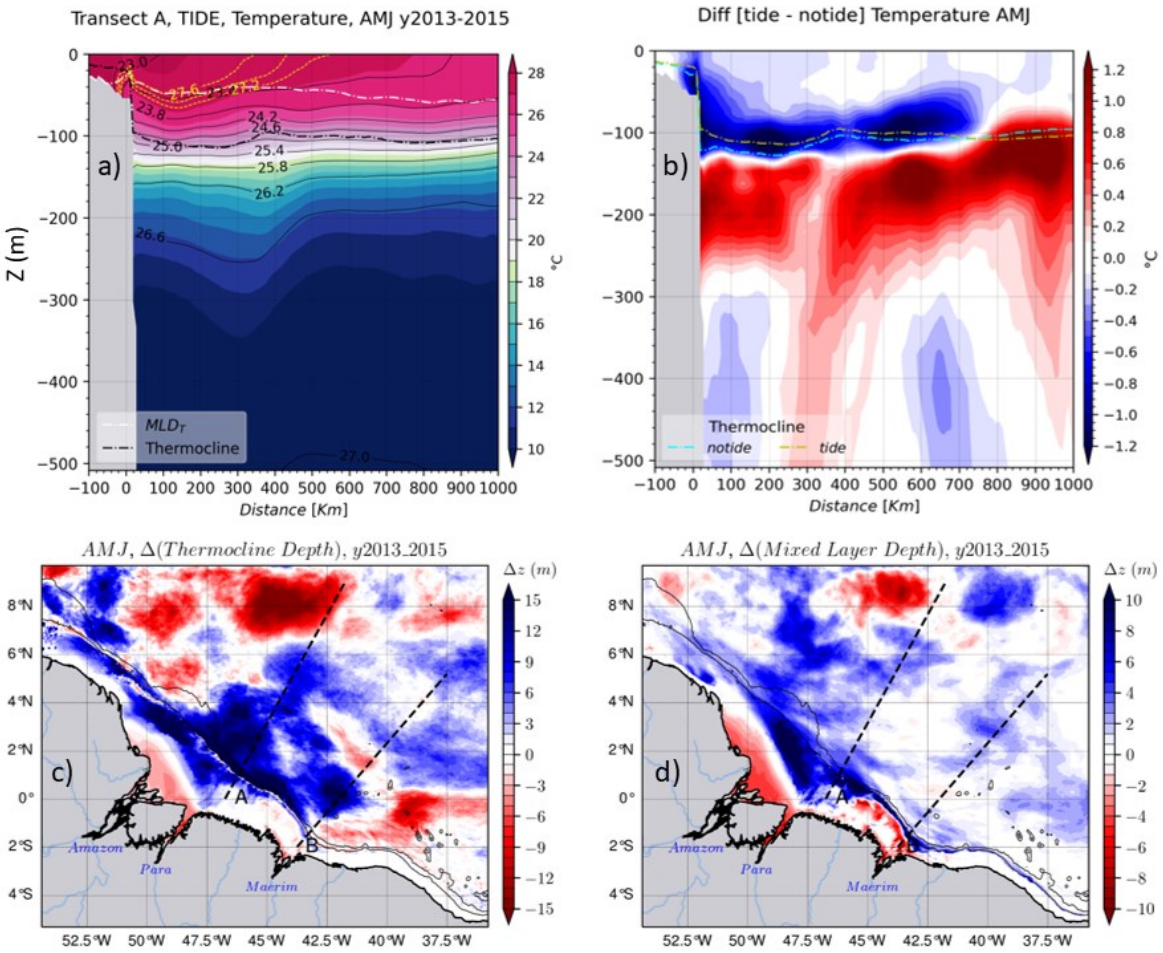

Figure 6: Some water mass properties for the AMJ season: (a) vertical section of the temperature of the tidal simulation following the transect A, the yellow dashed and the solid black lines are the temperature and density (σ_θ) isolines respectively, the black and white ticker dashed lines are the thermocline and MLD respectively, (b) the temperature anomaly for the same vertical section, yellow and cyan dashed lines are the thermocline depth for the tidal and non-tidal simulations respectively, (c) thermocline depth anomaly and (d) MLD anomaly for the whole domain. When the MLD or the Thermocline depth anomaly are colored in blue (vs red) it means that the tides rise (vs deepen) them.

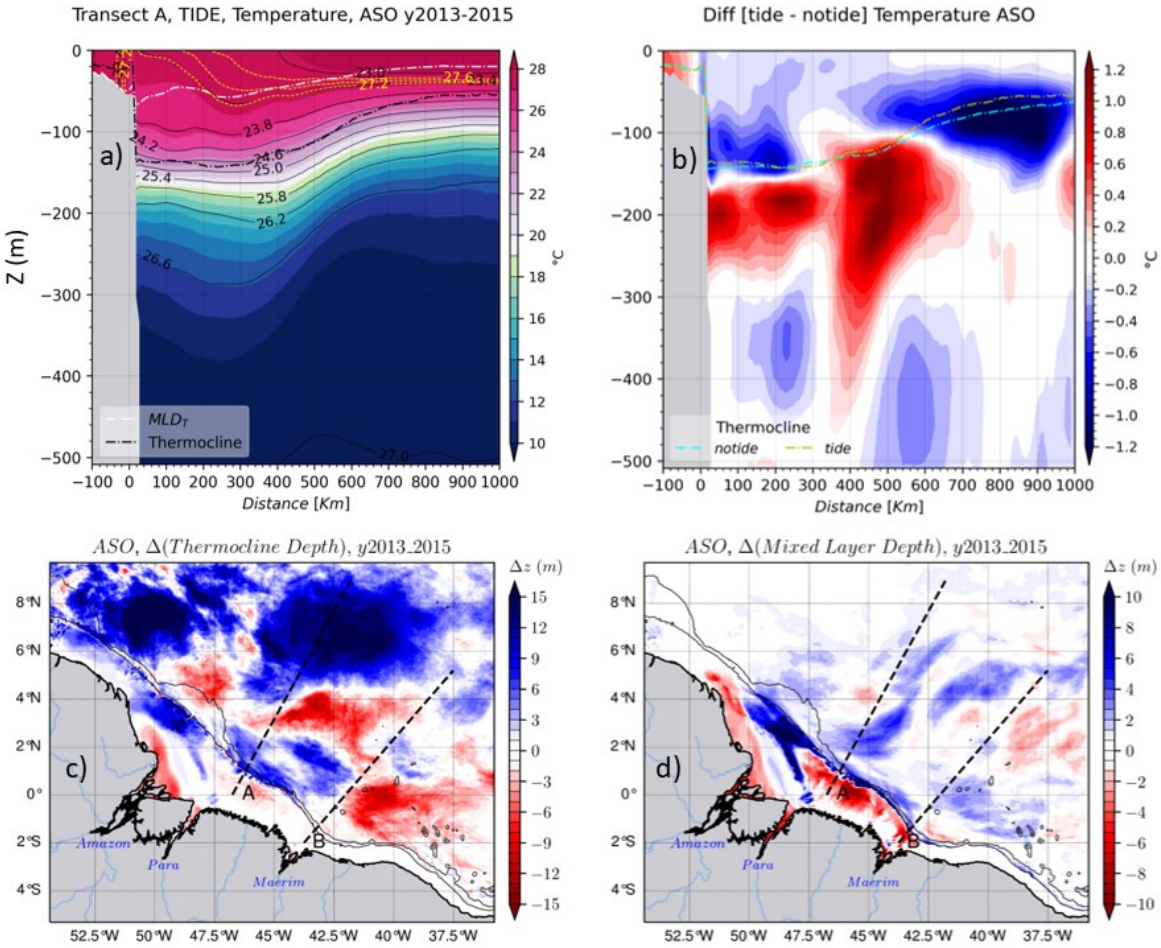

1182

1183 *Figure 7 : same as figure 6 but for the ASO season.*

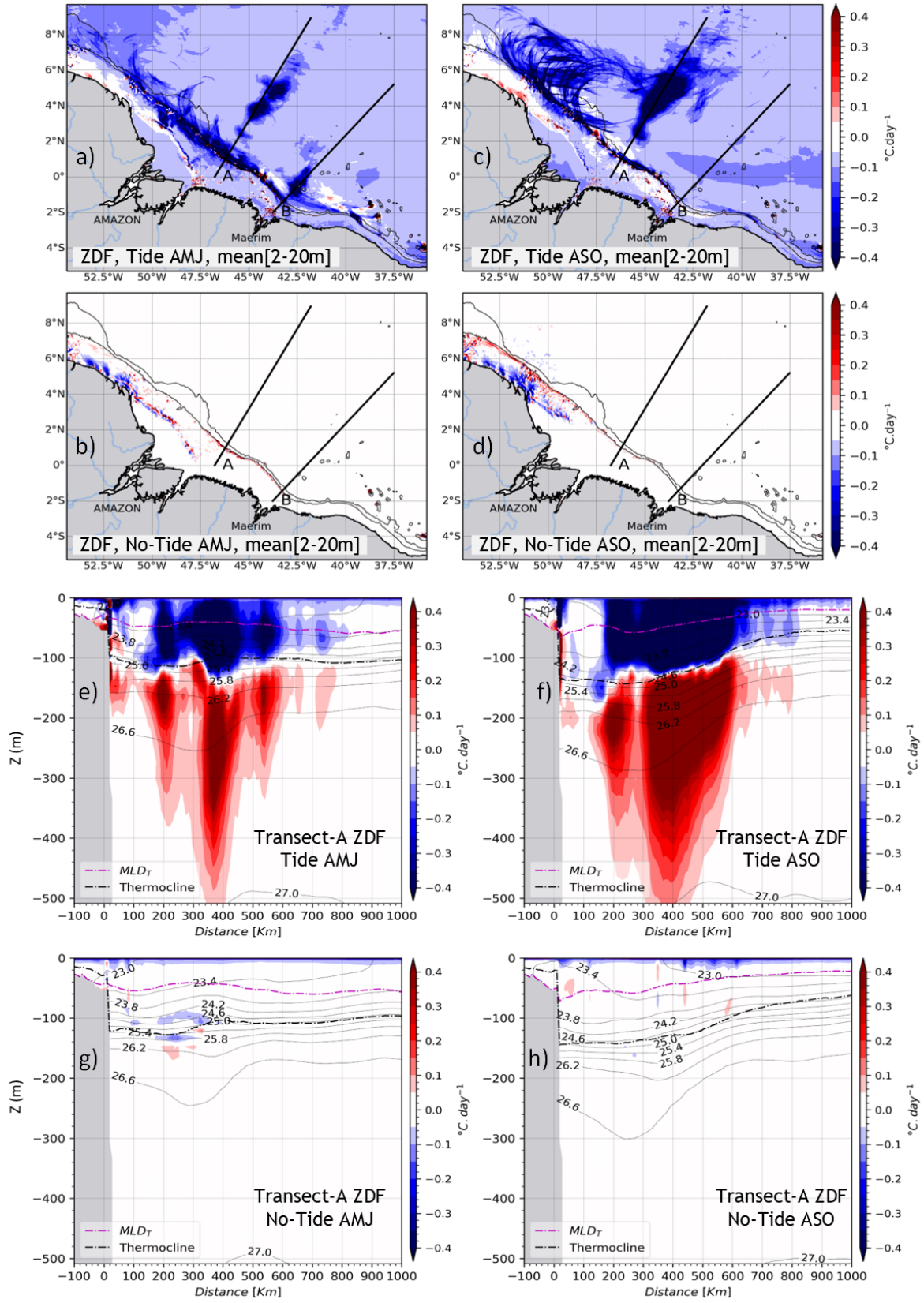

Figure 8: The vertical diffusion tendency of temperature (ZDF) for both seasons. The vertical mean between 2–20 m for AMJ season in tidal (a) and non-tidal (b) simulation; then for ASO

season in tidal (c) and non-tidal (d) simulations. Vertical sections of ZDF following the transect A for AMJ season in the tidal (e), for ASO season in non-tidal (f) simulations; then for AMJ season in the non-tidal (g) and for ASO season in the non-tidal (h) simulations. The black and magenta dashed lines are the thermocline depth and MLD respectively. Solid black lines represent the density (σ_θ) isocontours.

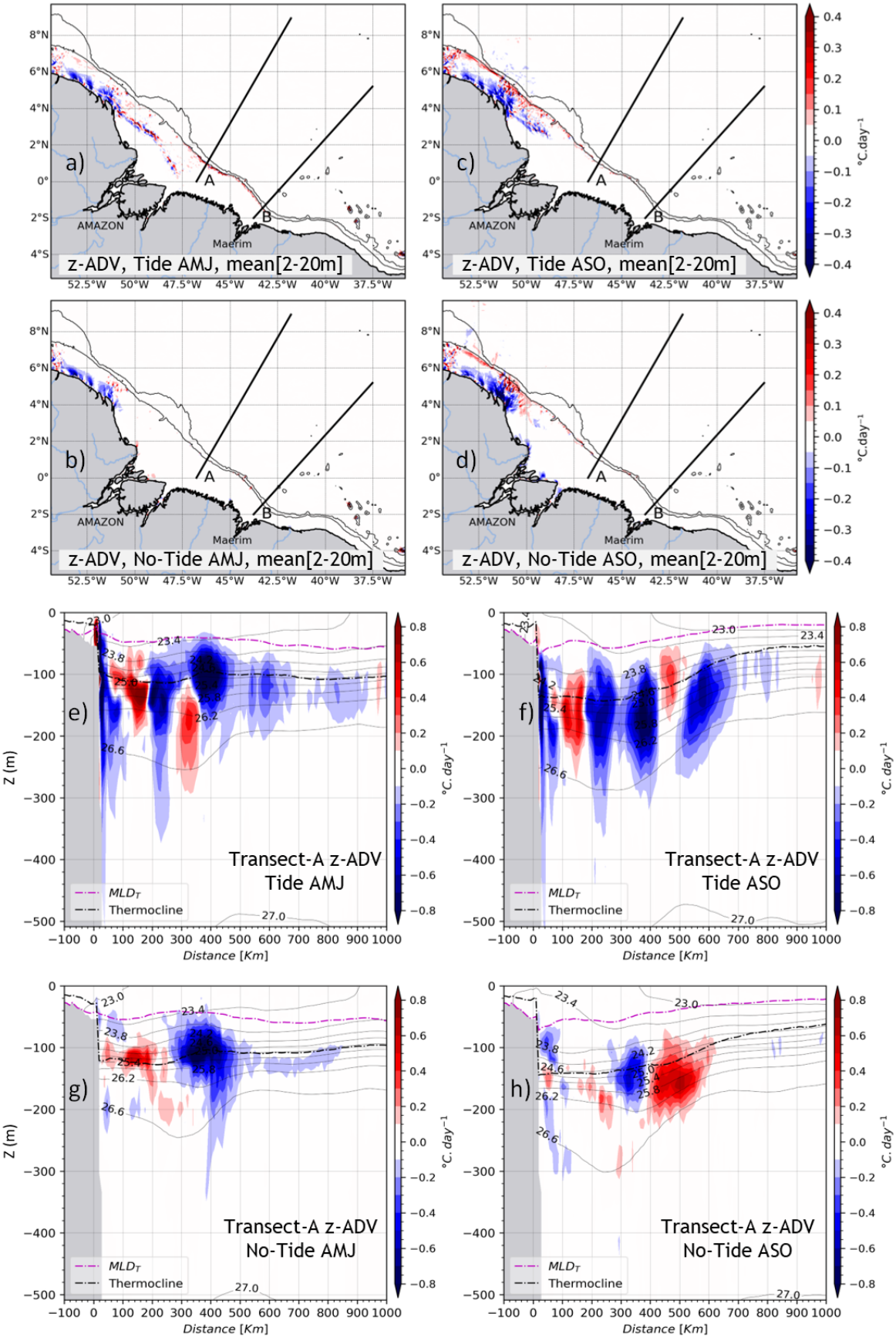
a)
z-ADV, Tide AMJ, mean[2-20m]
c)
z-ADV, Tide ASO, mean[2-20m]
b)
z-ADV, No-Tide AMJ, mean[2-20m]
d)
z-ADV, No-Tide ASO, mean[2-20m]
AMAZON
Maerim
A
B
°C.day⁻¹
e)
Transect-A z-ADV
Tide AMJ
f)
Transect-A z-ADV
Tide ASO
g)
Transect-A z-ADV
No-Tide AMJ
h)
Transect-A z-ADV
No-Tide ASO
Z (m)
Distance [Km]
MLD_T
Thermocline

1192

Figure 9: same as figure 8, but for the vertical advection tendency of temperature (z–ADV).

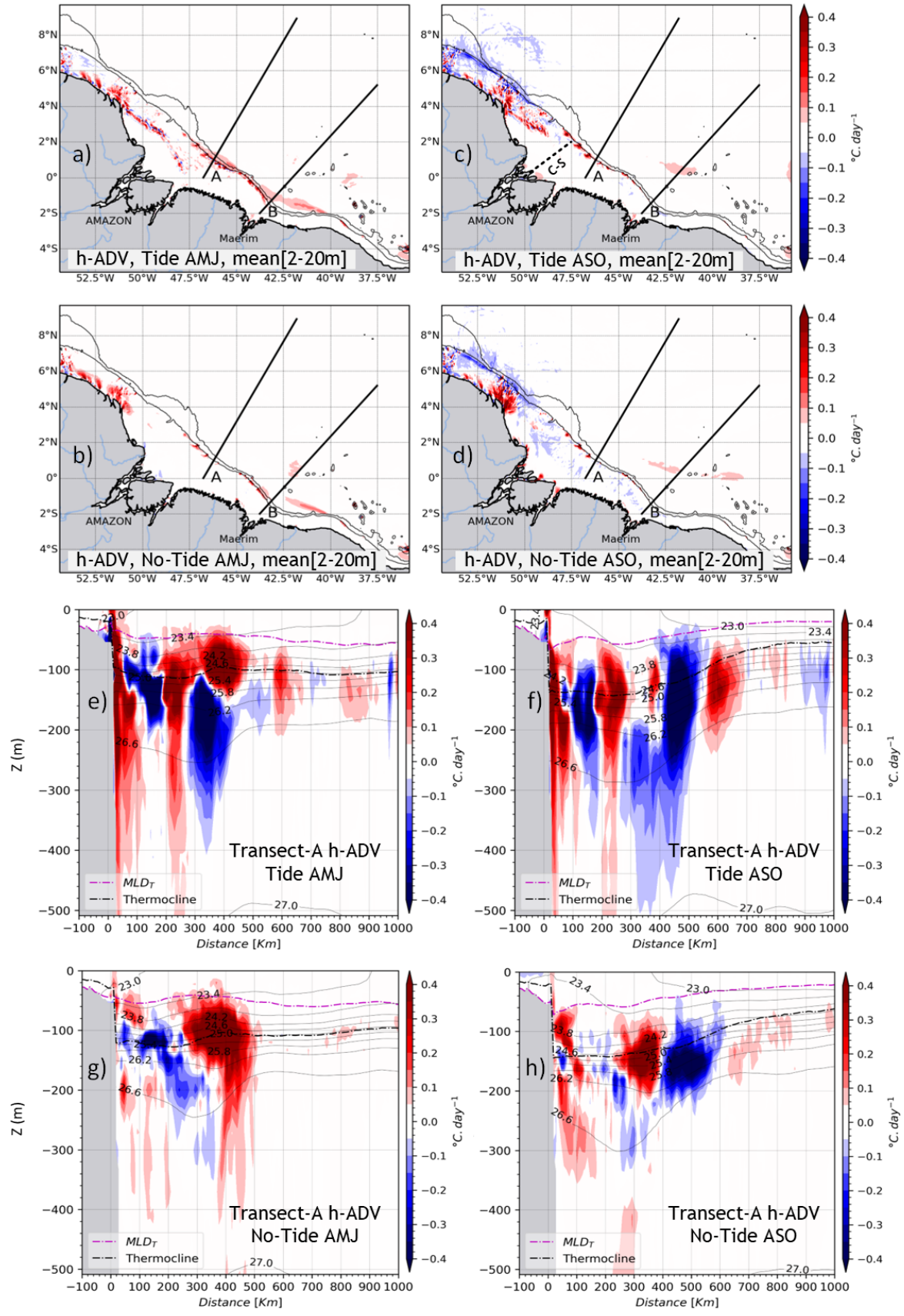
a)
h-ADV, Tide AMJ, mean[2-20m]
c)
h-ADV, Tide ASO, mean[2-20m]
b)
h-ADV, No-Tide AMJ, mean[2-20m]
d)
h-ADV, No-Tide ASO, mean[2-20m]
AMAZON
Maerim
A
B
C-S
°C. day⁻¹
e)
Transect-A h-ADV
Tide AMJ
f)
Transect-A h-ADV
Tide ASO
g)
Transect-A h-ADV
No-Tide AMJ
h)
Transect-A h-ADV
No-Tide ASO
MLD_T
Thermocline
Z (m)
Distance [Km]

1194

Figure 10: same as figure 8 but for the horizontal advection of temperature (h-ADV = x–ADV + y–ADV). The dashed line from the Amazon River mouth toward the outer shelf in the panel (b) indicates the cross-shore transect (C-S) used further on.

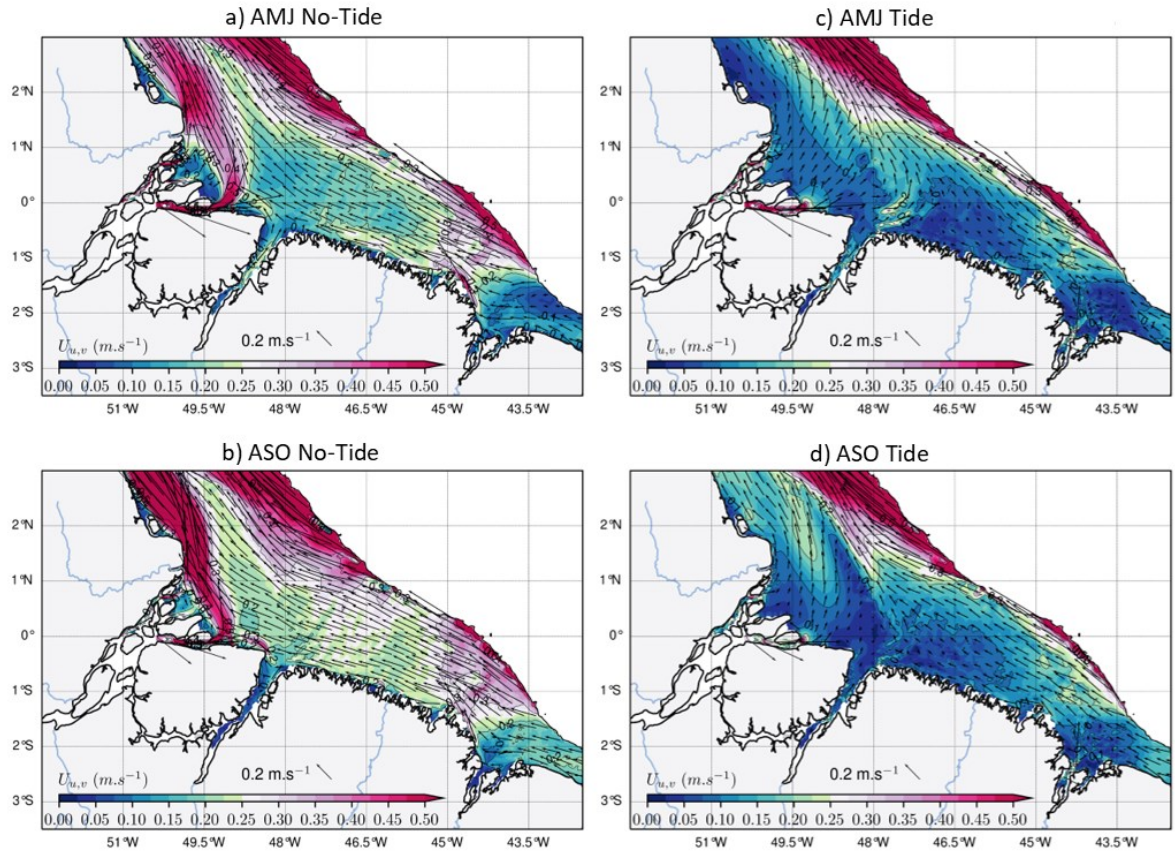

Figure 11: The seasonal mean of the current ($U_{u,v}$) at the shelf averaged between the surface and 50 m: the non-tidal simulation in the left panels and the tidal simulation in the right panels. The upper panels stand for the AMJ season, while the lower stand for the ASO season. The color shading is the modulus of the current and the black arrows represent its direction. Values beyond the 200 m isobath are masked.

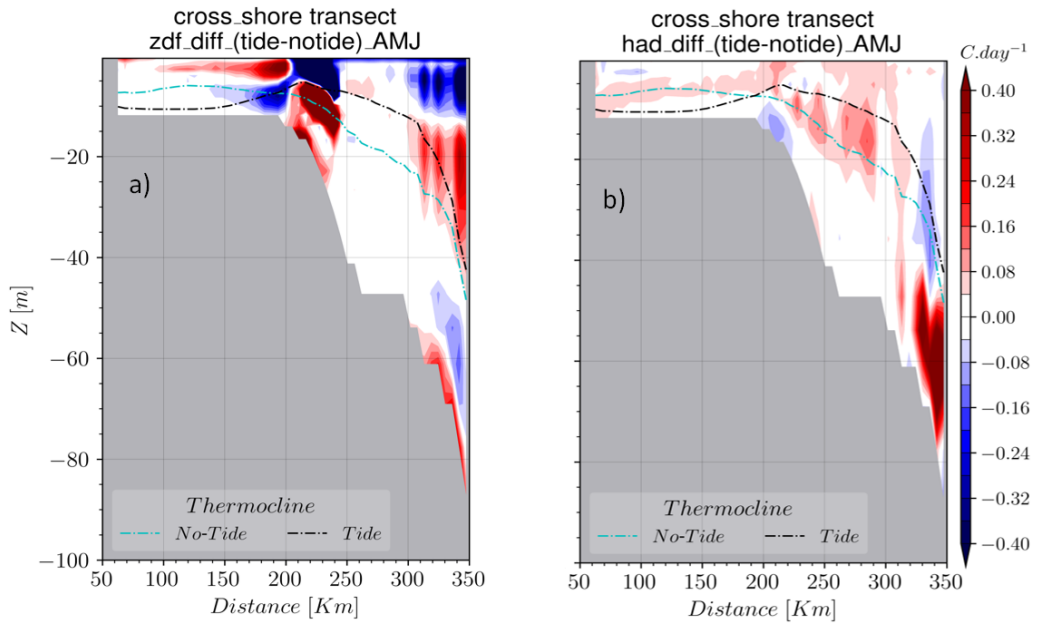

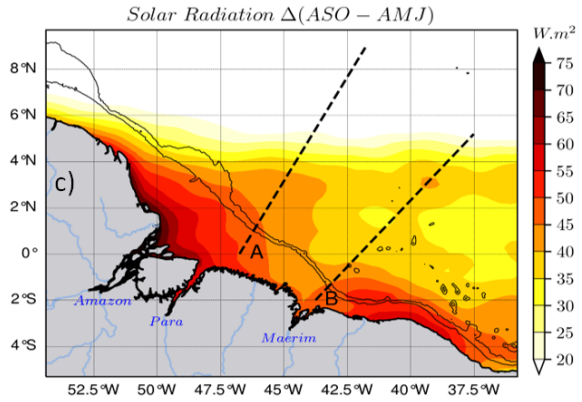

Solar radiation (Qs) increases in the ASO season:
> 30 W.m² offshore
> 60 W.m² over the shelf

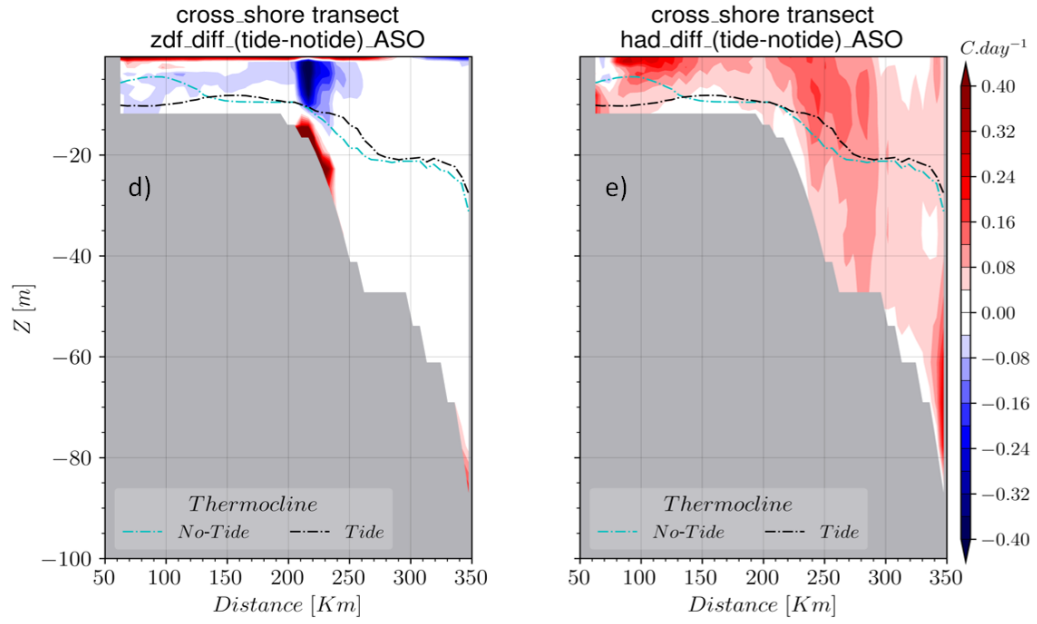

1205

Figure 12: The cross-shore transect of ZDF anomaly for (a) AMJ and (b) ASO seasons, then for h-ADV anomaly for (d) AMJ and (e) ASO seasons ; (c) Difference in solar radiation between ASO and AMJ seasons. Solar radiation increases during the ASO season, with greater intensity on the shelf.

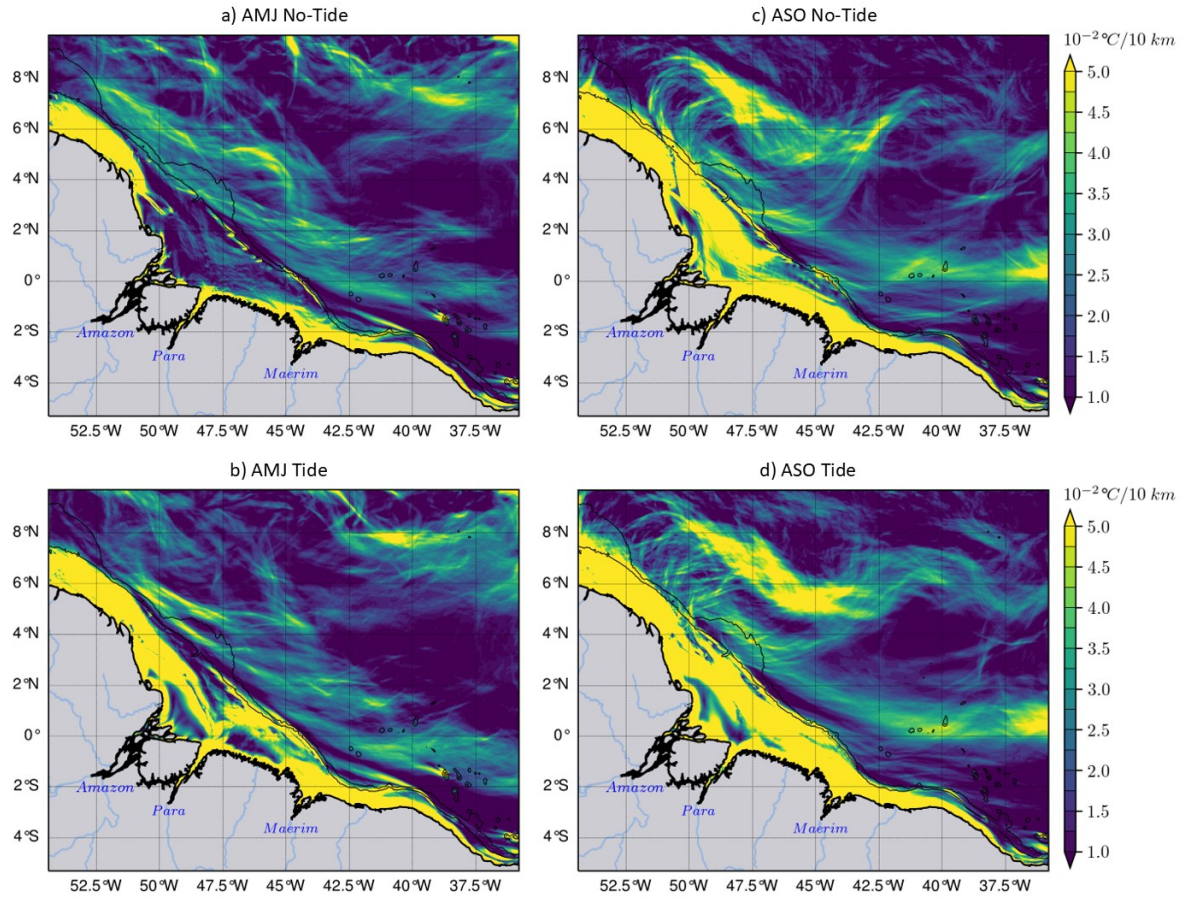

Figure 13 : The horizontal gradient of the Temperature (∇T) averaged between 2–20 m : the AMJ season in the left panels and ASO season in the right panels, the simulations without the tides in the upper panels, and with tides in the lower panels. During the ASO season, the NBC retroflects and eddy activity intensifies in the north-west. Therefore, ∇T emphasizes eddy-like fronts at the same location as eddy-like patterns in ZDF (see Fig.8b).